Lower Hybrid Cavities and Other Plasma Phenomena in the Subauroral Region

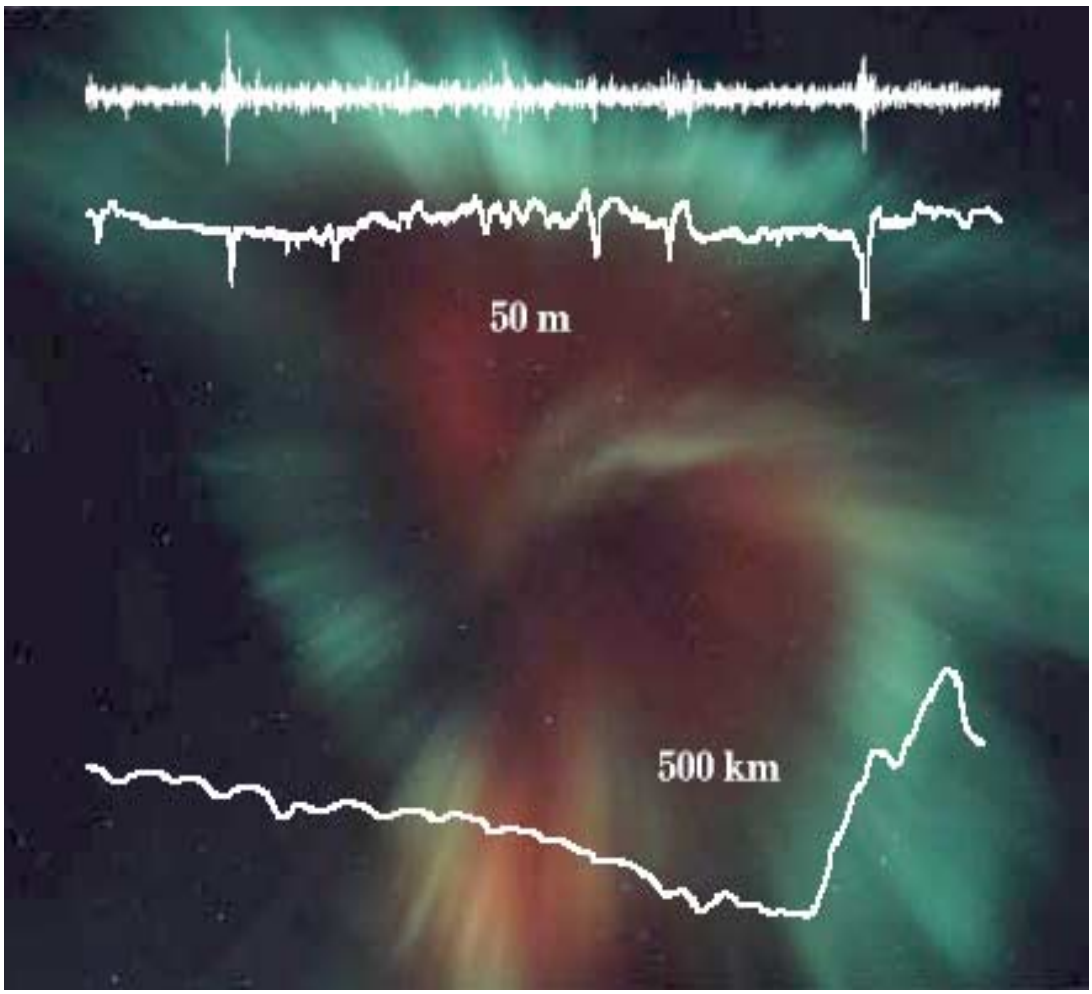

Solveig H. Høymork
Swedish Institute of Space Physics, Kiruna

Lower Hybrid Cavities and Other Plasma Phenomena in the Subauroral Region

Solveig H. Høymork
Swedish Institute of Space Physics
Kiruna

February 2001

Cover:
The cover shows examples of lower-hybrid cavities (scale size 50 m) and a large-scale cavity (scale size 500 km). Background is an auroral corona (photo taken by Masatoshi Yamauchi).

Cover design by Solveig H. Høymork under artistic advice from Björn Gustafsson.

Doctoral thesis at the Swedish Institute of Space Physics,
Kiruna, 2001
Lower Hybrid Cavities and Other Plasma Phenomena in the Subauroral Region
Typeset by the author in LaTeX.

IRF Scientific Report 276
ISSN 0284-1703
ISBN 91-7191-996-1
Printed at the Swedish Institute of Space Physics
Box 182, SE-981 28, Kiruna, Sweden
February 2001

Abstract

This thesis provides a discussion of lower hybrid cavities, large-scale cavities, and ion clouds found in the subauroral region of the upper ionosphere/lower magnetosphere. All these phenomena show localized changes in e.g density, particle flux, and/or wave activity. Lower hybrid cavities (LHCs) are characterized by an enhanced lower hybrid wave enclosed inside a localized small scale (scale size ~ 50 m perpendicular to the magnetic field) density depletion. A large number of these LHCs are observed by the Freja satellite. This thesis presents statistical investigations of their distribution and shape, and discuss their relation to ion heating. The cavities are found to be Poisson-distributed in space, they have a cylindrically symmetric Gaussian shape, an average density perturbation of -2.1%, and they do not seem to be correlated with strong ion heating.

Large-scale cavities, i.e., the auroral density cavities (ADCs) and the low-latitude cavities (LLCs) observed by the Astrid-2 satellite are discussed in terms of solar illumination and K_p-index. ADCs are observed solely in the non-illuminated ionosphere (polar winter) while LLCs also occur in the illuminated ionosphere. The fact that ADCs are preferably observed during low K_p indicates that the lowest altitude of these cavities is close to the Astrid-2 altitude (1000 km) since these cavities show an even distribution of occurrence for all K_p above an lower altitude boundary, and the altitude of this boundary is decreasing for decreasing K_p.

This thesis also discusses ion clouds observed by the Astrid-2 satellite. These are local populations of sub-keV ions with higher density and flux than the ambient hot plasma. Three different sources for these ion clouds are discussed; (1) substorm injection, (2) upward flowing ions from the conjugate hemisphere, and (3) direct magnetosheath plasma injection. However, none of them seems to fully account for the observations.

Sammanfattning

Denna avhandling behandlar lägre hybridkaviteter, storskaliga kaviteter och jonmoln som observerats på ekvatorsidan av norrskens-/sydskens-zonen i den övre jonosfären och nedre magnetosfären. Alla dessa fenomenen är lokala förändringar i till exempel täthet, partikelflöde och/eller vågaktivitet. Lägre hybridkaviteter (LHC) karakteriseras av att lägre hybridvågor ökar i amplitud i småskaliga täthetsminima (kaviteter) med karakteristisk storlek vinkelrätt mot magnetfältet på ungefär 50 meter. En stor mängd sådana LHCer har observerats av Frejasatelliten och här presenteras en statistisk undersökning av deras fördelning och form och också en diskussion om deras relation till jonupphettning. Det visas att kaviteterna är Poissonfördelade i rummet, att de har en cylindriskt symmetrisk Gaussisk form och en genomsnittlig täthetsminskning på 2.1%. Det verkar inte som om de är korrelerade med stark jonupphettning.

Storskaliga kaviteter, norrskens/sydskens-täthetskaviteten (ADC) och låglatitudkaviteten (LLC), som observerats med satelliten Astrid-2 diskuteras i relation till solbelysning och K_p-index. ADC observeras bara i en icke-solbelyst jonosfär, medan LLC också observeras när jonosfären är solbelyst. Det faktum att ADCer observeras huvudsakligen vid låga K_p indikerar att Astrid-2's höjd (1000 km) är nära den lägsta höjden för dessa kaviteter eftersom andra observationer har visat att dessa kaviteter för alla K_p har en jämn höydfördelning

ovanför en lägre höydgräns, och att höyden för denna lägre gräns sjunker med sjunkande K_p.

Så kallade jonmoln, som observerats av Astrid-2 satelliten, diskuteras också. Dessa är lokala koncentrationer av sub-keV joner som har högre täthet och flöde än det varma bakgrundsplasmat. Tre olika källor för dessa jonmoln presenteras: (1) substormsinjektion, (2) jonflöde från den motsatta hemisfären och (3) direkt injektion av plasma från magnetoskiktet, men ingen av dem kan förklara observationerna fullständigt.

Sammendrag

Denne avhandlingen presenterer nedre hybridkaviteter, storskala kaviteter og ionskyer som er observert på ekvator-siden av nordlys-sonen i den øvre ionosfæren/nedre magnetosfæren. Alle disse fenomenene er lokale forandringer i f.eks. tetthet, partikkelfluks og/eller bølgeaktivitet. Nedre hybridkaviteter (LHCer) er karakterisert ved en økning i amplituden av nedre hybridbølger inne i lokale småskala (karakteristisk størrelse på tvers av magnetfeltet er ~ 50 meter) tetthets fordypninger (kaviteter). En stor mengde slike LHCer er observert med Freja satellitten og her presenteres statistiske undersøkelser av deres fordeling og form og også en diskusjon av deres relasjon til ion opphenting. Det blir vist at disse kavitetene er Poisson-fordelte i rommet. De har en sylindrisk, symmetrisk, Gaussisk form og en gjennomsnittlig tetthets fordypning på 2.1%. Det virker ikke som de er korrelert med sterk ionopphetning.

Storskala kaviteter, nordlys/sørlys tetthetskaviteten (ADC) og lavlatitudekaviteten (LLC), observert med Astrid-2 satelliten blir også diskutert i relasjon til sol belysning og K_p-indeks. ADC er bare observert under en mørk ionosfære, mens LLC også er observert under en solbelyst ionosfære. Andre observasjoner har vist at ADCer er jevnt fordelt for alle K_p ovenfor en nedre grense i høyde og at denne grensen synker med synkende K_p. Med Astrid-2 er ADCer observert hovedsaklig under lav K_p og dette indikerer derfor at Astrid-2's høyde (1000 km) er nær den nederste høyden for disse kavitetene.

Såkalte ionskyer, observert av Astrid-2 satellitten, blir også diskutert. Disse er lokale konsentrasjoner av sub-keV ioner som har høyere tetthet og fluks enn det varme bakgrunnsplasmaet. Tre ulike kilder for disse ionskyene blir presentert; (1) substorm injeksjon, (2) ioner som flyter oppover fra den motsatte hemisfæren og (3) direkte injeksjon av plasma fra magnetosjiktet. Men ingen av dem kan fullstendig forklare observasjonene.

Keywords: space, plasma, density cavities, lower hybrid waves, particle precipitation and energization, satellite observations.

Til mamma, pappa og Amund

"Kanskje vil der gå både vinter og vår,
og neste sommer med, og det hele år;-
men en gang skal du komme, det vet jeg visst;
og jeg kan nok vente, for det lovte jeg sist,..."

(Solveig's song, Peer Gynt)

Contents

Publications

Papers that are included in this thesis:

I S. H. Kjus, H. L. Pécseli, B. Lybekk, J. Holtet, J. Trulsen, H. Lühr and A. Eriksson, *Statistics of Lower-Hybrid Wave Cavities Detected by the FREJA Satellite*, Journal of Geophysical Research A11, 103, 26 633 – 26 647, 1998.

II S. H. Høymork, H. L. Pécseli, B. Lybekk, J. Trulsen and A. Eriksson, *Cavitation of Lower–Hybrid Waves in the Earth's Ionosphere; a model analysis*, Journal of Geophysical Research A8, 105, 18 519 – 18 535, 2000.

III S. H. Kjus, L. Eliasson, H. L. Pécseli, B. Lybekk, J. Holtet, P. Norqvist, J. Trulsen, and A. Eriksson, *Lower Hybrid Waves in the Earths Upper Ionosphere - Wave Cavitation and Ion Heating*, Physics of Space Plasmas 15, 209 – 214, 1998.

IV S. H. Høymork, R. Lundin, Y. Narita, O. Norberg, and D. Winningham, *Statistical study of large scale density cavities observed by ASTRID-2*, submitted to Annales Geophysicae 2000.

V S. H. Høymork, M. Yamauchi, Y. Ebihara, Y. Narita, O. Norberg, and D. Winningham, *Dense ion clouds of 0.1-2 keV ions inside the CPS-region during low Kp observed by Astrid-2*, submitted to Annales Geophysicae 2000.

Related conference proceedings that are not included in the thesis:

S. H. Kjus, H. L. Pécseli, B. Lybekk, J. Holtet, J. Trulsen and A. Eriksson, *Solitary Waves in the Earths Upper Ionosphere*, Solitons and Coherent Structures in Physics and Biology, 30 May - 3 June 1997.
(http://serv1.imm.dtu.dk/documents/users/mps/SOLPHYS/proceedings/Pecseli/)

S. H. Kjus, H. L. Pécseli, B. Lybekk, J. Holtet, J. Trulsen and A. Eriksson, *Lower Hybrid Waves and Wave Cavitation in the Earths upper Ionosphere*, The 24th Annual European Meeting on Atmospheric Studies by Optical Methods, Andenes, Norway, 18-22 August 1997.

S. H. Høymork, H. L. Pécseli, B. Lybekk, J. Trulsen and A. Eriksson, *The shape and evolution of lower hybrid density cavities observed by Freja.* Phys. Chem. Earth 1-3, 26, 213 – 217, 1999. (refereed)

H. L. Pécseli, S. H. Høymork, B. Lybekk, J. Trulsen and A. Eriksson, *Solitary waves in the earth's upper ionosphere.* Journal of Technical Physics, 41, 391 – 400, 2000. Proceedings of the XXIV ICPIG-conference, Warsaw.(refereed)

S.H. Høymork, Y. Narita, M. Yamauchi, Y. Ebihara, O. Norberg, D. Winningham, *Dense plasma cloud of 0.1 - 1 keV ions inside the early morning CPS region observed by Astrid-2.* Proceedings of the Fifth International Conference on Substorms, 16-20 May 2000, St. Petersburg, Russia.

1
Introduction

The near Earth space is fascinating with a plethora of different plasma physical phenomena. Localized changes in the plasma that stand out from the background environment in density, energy, wave activity or other characteristics attract scientific attention. In fact, some localized phenomena, like the solitary lower hybrid waves and plasma density depletions (Paper I, II and III), show an almost textbook-like appearance. These are wave packets enclosed in local, small-scale (a scale size of 50 m perpendicular to the magnetic field) density cavities. Other density cavities, with varying spatial scales, appear in many different regions in the near Earth space. Large scale cavities, the auroral cavity and the low latitude cavity (Paper IV) have a scale size of some hundred to some thousand km and appear, correspondingly, inside the auroral precipitation region and on its equatorward boundary. A different localized and enclosed plasma phenomenon is the ion clouds (Paper V). These are local ion populations of higher density and flux than the ambient hot plasma, that are observed in the CPS (Central Plasma Sheet) region in the morning-side upper ionosphere.

Most of the phenomena discussed in this thesis (with the exception of the auroral density cavities) are observed equatorward of the so-called auroral oval, i.e., in the sub-auroral region. The auroral oval is the oval-shaped area where aurora appears. Its position is dynamic and varies with solar activity.

1.1 Organization of this thesis

This thesis begins with a general introduction to relevant basic mechanisms and definitions. A large part of this introduction is textbook knowledge that can be found in plasma physics textbooks [e.g. Chen, 1984; Goldston and Rutherford, 1995] or space physics textbooks [e.g. Lyons and Williams, 1984], but some pieces are newer findings or unestablished theories. References to some relevant studies will be given for the latter. After the introduction, summaries of the five core papers are included. The Appendix consists of background material (Appendix B and C), but also some new results that are not included as papers (Appendix A and D). The five core papers are found at the end.

The introduction is organized as follows: section 1.2 gives a brief introduction to plasma and the relevant plasma environment, sections 1.3–1.5 briefly present particle motion and particle regions in the near Earth space, sections 1.6–1.8 give an overview of waves and density cavities, and section 1.9 presents the measurement platforms (two satellites) used in this work.

1.2 The plasma environment

More than 99% of the known matter in the universe is in the plasma state. A plasma can be described as an ionized gas where a significant fraction of the atoms are dissociated into positive ions and negative electrons. The charged particles interact with electric and magnetic fields and the behavior of a plasma is thus different from a neutral gas.

Even though plasma is rather rare on the Earth's surface, the surrounding space environment consists to a large extent of plasma. The plasma population nearest the Earth is the ionosphere which reaches from ∼80 km up to ∼1000 km above the Earth's surface. Here particles from space interact with the particles coming from the atmosphere, giving rise to a diversity of phenomena. The most easily visible example is the auroral light which is frequently seen at high latitudes.

The near Earth space plasma has been extensively studied under the framework of solar-terrestrial physics. There are many reasons for studying solar-terrestrial physics. Some of them are:

- basic exploration of our near Earth space environment to understand how it works
- the magnetospheric plasma can be used as a large plasma laboratory both for passive and active experiments. This plasma environment has the advantage of being larger in spatial scale than plasma laboratories on the Earth and hence has less edge effects.
- it is important to understand the space environment and fundamental mechanisms to prevent hazards to satellites and astronauts, and also to radio communication and a number of technical systems on the ground.
- in-situ measurements in the near Earth space environment might give results that also apply to other environments in the Universe.

The work presented herein concentrates on only a small part of the solar-terrestrial plasma. It gives a discussion of some chosen phenomena that are seen in data from two satellites in the upper ionosphere/lower magnetosphere (1000 - 1700 km). The background plasma at 1700 km altitude in the subauroral zone has a temperature of around 1000 K and a density of about $5 \cdot 10^2$ cm^{-3}.

1.3 Motion of a charged particle in the geomagnetic field

The magnetosphere is the region of space where the Earth's magnetic field, the geomagnetic field, dominates space plasma behavior. The following subsections give an overview of some of the basic features that control the motion of a charged particle in magnetic and electric fields.

1.3.1 Drift motion

A charged particle in a magnetic field, $\mathbf{B}$, will be influenced by the Lorentz force:

$$\mathbf{F} = q\mathbf{v} \times \mathbf{B}, \tag{1.1}$$

where $\mathbf{v}$ and q are the velocity and charge of the particle. This force will make the particle gyrate around the magnetic field with a radius, the Larmor radius, r_L, given by

$$r_L = \frac{mv_\perp}{|q|B}, \tag{1.2}$$

and with a gyro frequency (or cyclotron frequency) given by

$$\omega_c = \frac{|q|B}{m} \tag{1.3}$$

where m and $v_\perp$ are the mass of the particle and the velocity component perpendicular to the magnetic field. Since the Lorentz force is proportional to the charge (see Eq. 1.1) it will cause ions and electrons to gyrate in opposite directions. From Eq. 1.2 and 1.3 we see that ions will have larger Larmor radii and lower cyclotron frequencies compared to electrons with the same velocity and in the same magnetic field. Note that the force in Eq. 1.1 does not affect the particle motion parallel to the magnetic field.

The center of this gyration motion is called the guiding center. It is usually easier to describe the motion of a charged particle in a magnetic field by the motion (drift) of its guiding-center than to describe the true particle trajectory. The only difference is that the gyro-motion is subtracted in the guiding-center description.

An electric field, $\mathbf{E}$[1], exerts a force on a charged particle given by

$$\mathbf{F} = q\mathbf{E}. \tag{1.4}$$

If the electric field has a component parallel to the magnetic field, this will result in an acceleration of the particle parallel to the magnetic field. An electric field perpendicular to the magnetic field causes, on the other hand, a particle-drift perpendicular to both the magnetic and electric fields, the $\mathbf{E} \times \mathbf{B}$-drift:

$$\mathbf{v}_E = \frac{\mathbf{E} \times \mathbf{B}}{B^2}. \tag{1.5}$$

The actual particle motion is sketched in Figure 1.1 and can be considered to be the summation of a gyro-motion around the magnetic field, with a radius determined by the magnetic field (Eq. 1.2) and a drift with a velocity across magnetic field lines determined by both $\mathbf{E}$ and $\mathbf{B}$ (Eq. 1.5).

Inhomogeneous or time-varying magnetic fields will also give rise to particle drifts. A gradient in the magnetic field causes a ∇B-drift and a curvature in the magnetic field causes a curvature-drift, as illustrated in Figure 1.1. The formulas for these drifts are listed in Table 1.1. Temporal and spatial changes in the electric field also affect particle motion through the polarization drift and the finite-Larmor-radius effect.

It must be noted that the drift formulas given in Table 1.1 are valid only when the temporal and spatial changes of the magnetic field are small compared to the cyclotron frequency and Larmor radius. Under these conditions the gyro-motion and the three drifts in Table 1.1 give rise to three adiabatic invariants.

[1]Examples of electric fields in the magnetosphere are the convection electric field and double layers, where the first is perpendicular and the latter is parallel to the geomagnetic field. Double layers have almost no contribution to drift in the magnetosphere.

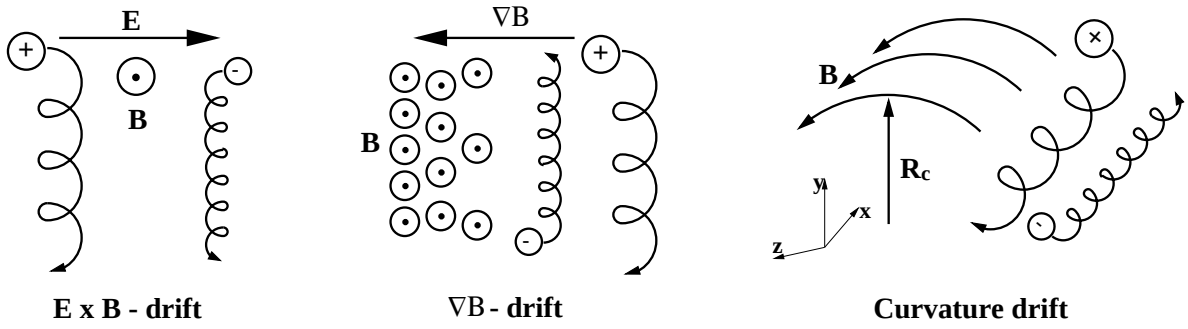

Figure 1.1: Drifts of charged particles in a magnetic field.

Table 1.1: Some guiding center drifts in a magnetic field. ($\mathbf{R}_c$ is the radius of curvature of the magnetic field.)

$\mathbf{E}\times\mathbf{B}$-drift	$v_E = \frac{\mathbf{E}\times\mathbf{B}}{B^2}$
∇B-drift	$v_{\nabla B} = \pm\frac{1}{2}v_\perp r_L \frac{\mathbf{B}\times\nabla\mathbf{B}}{B^2}$
Curvature drift	$v_R = \frac{mv_\parallel^2}{q}\frac{\mathbf{R}_c\times\mathbf{B}}{R_c^2 B^2}$

1.3.2 Adiabatic invariants

From classical mechanics we know that for a system in periodic motion the action integral, $\oint pdq$, taken over one period of the motion will be constant (p and q are here the momentum and coordinate). If a slow change is made to the system the motion is not quite periodic but the constant of the motion will still not change. The motion of a gyrating particle in the geomagnetic field can be considered to be a periodic motion forming the action integral in this sense if the variations of the magnetic field are small compared to the cyclotron frequency and Larmor radius. The action integral is in this case given by

$$\oint pdq = \oint mv_\perp r_L d\theta = 2\pi r_L m v_\perp = 4\pi\frac{m}{|q|}\mu, \tag{1.6}$$

where μ is the magnetic moment of the particle, given by

$$\mu = \frac{mv_\perp}{2B}. \tag{1.7}$$

We see from Eq. 1.6 that since the action integral is constant the magnetic moment is also a constant of the motion. The magnetic moment is known as the *first adiabatic invariant*.

Conservation of the total kinetic energy of the particle gives

$$\varepsilon_{tot} = \varepsilon_\parallel + \varepsilon_\perp = \frac{1}{2}mv_\parallel^2 + \frac{1}{2}mv_\perp^2 = \frac{1}{2}mv_\parallel^2 + \mu B = \text{constant}, \tag{1.8}$$

by inserting the first adiabatic invariant (Eq. 1.7). This implies that a charged particle moving into a converging magnetic field (stronger B) will lose parallel velocity, and if $B > \varepsilon_{tot}/\mu$ the

particle "mirrors" at the point where $B = \varepsilon_{tot}/\mu$, and travels back along the field line to where it came from. The reflection point is called the "magnetic mirror point" and it will thus be different for different particle velocities. As a result of this, a particle moving in a dipole-like field, such as the geomagnetic field, will be trapped between the two hemispheres, provided that the magnetic mirror points are at high enough altitude. Particles that enter the lower ionosphere will interact with atmospheric (ionospheric) particles and will not mirror back into the magnetosphere. Whether a particle is mirrored or lost to the atmosphere is predicted by its pitch-angle, α. It is given by:

$$\sin(\alpha) = \frac{v_\perp}{v}, \tag{1.9}$$

where $v_\perp$ and v are the perpendicular and total velocities of the particle. Particles that have a mirror point as low as the lower ionosphere will be lost there, i.e. the particles will collide instead of mirror back. These are the particles which are inside the *loss cone*, and they have

$$\sin(\alpha_0) < \sqrt{\frac{B_0}{B_m}}, \tag{1.10}$$

from the conservation of energy and magnetic moment, μ, for particle motion between equator, with magnetic field B_0 and pitch-angle α_0, and its mirror point, with magnetic field B_m.

The *second adiabatic invariant* is concerned with the motion of a trapped particle between two magnetic mirrors. This is a nearly periodic motion and the second adiabatic invariant is given by

$$J = \int_a^b v_{||} ds = \text{constant}, \tag{1.11}$$

where $v_{||}$ is the parallel velocity of the particle guiding center, and the integration is over the bounce path between the two mirror points (a and b).

The relatively slow drift of the guiding center of the trapped particle around the Earth (east-west direction) can also be considered a periodic motion. This gives the *third adiabatic invariant* which is the total magnetic flux enclosed by the drift surface.

Conservation of all three adiabatic invariants results in trapped particles in the geomagnetic field, forming the *radiation belts*. These ions and electrons undergo a combined curvature and gradient drift so that ions drift westward and electrons drift eastward giving a current in the westward direction. This *ring current* is located between about 2-7 Earth radii.

1.4 Particle populations in the magnetosphere

The Earth has a dipole-like magnetic field that is compressed by the dynamic pressure of the solar wind (particles streaming from the sun) on the day side and dragged out to a long tail on the night side, as illustrated in Figure 1.2. The area of space where the geomagnetic field dominates forms a cavity in the solar wind, called the magnetosphere. The magnetosphere consists of a variety of different plasma populations as illustrated in Figure 1.2. Table 1.2 gives typical densities and temperatures in some of these regions.

We usually divide the geomagnetic field lines into two groups: closed field lines and open field lines. The closed field lines are connected to the Earth at both ends whereas the open field lines are connected to the Earth at one end and to the interplanetary magnetic field at the other.

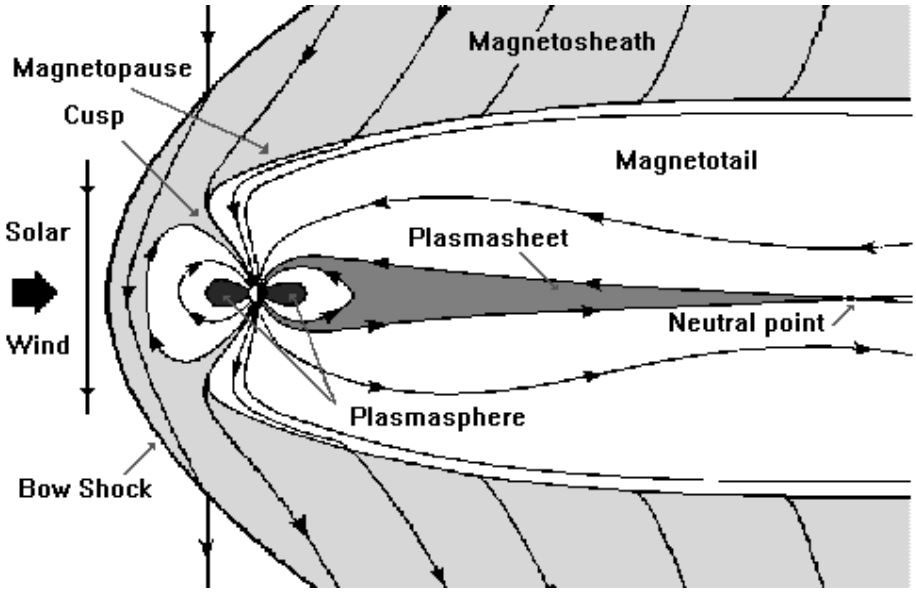

Figure 1.2: Particle regions in the magnetosphere: The magnetopause is the outer boundary of the magnetosphere ($\sim 10\ R_E$), i.e. the boundary between the interplanetary magnetic field and the Earth magnetic field. A few Earth radii outside the magnetopause is the bow shock, a shock front between the supersonic solar wind and the magnetosphere. Between the bow shock and the magnetopause is the magnetosheath. The extended geomagnetic field lines on the night side form the magnetotail. This region contains magnetic field lines in opposite directions from the northern and southern hemispheres. The boundary between them, where the magnetic field strength is nearly zero, is called the neutral sheet. The part of the magnetosphere that is closest to the Earth is the plasmasphere and its outer boundary is the plasmapause. In the equatorial plane on the nightside is the plasmasheet. It follows the magnetic field lines to high latitudes close to the Earth and its high latitude boundary is the plasma sheet boundary layer. Magnetic field lines that originate from the day-side of the cusp diverges both toward subsolar region, nightside, and magnetosheat. (Image by the Space Physics Group, Oulu, Finland at http://www.oulu.fi/ spaceweb/textbook/.)

1.4.1 Geomagnetic storms and magnetospheric substorms

Geomagnetic storms are large global changes in the geomagnetic field in near Earth space associated with enhancement of the ring current. They last from one day to several days. The strengths of geomagnetic storms are usually measured by the D_{st}-index (storm level is below $\sim$-30 nT).

Magnetospheric substorms are large-scale magnetospheric configuration changes which produce auroral breakups and short-time distortions in the horizontal component of the ground geomagnetic field (several hundred nT change in from a few to ten minutes). These magnetic distortions are caused by ionospheric electric currents in the polar regions which are associated with a sharp change of the current system in the near Earth magnetotail. Measurements and simulations in the magnetosphere show that the plasma sheet (see Figure 1.2) becomes very thin during substorm growth phase. This results in a temporary more stretched magnetic field on the nightside. Substorm onset is characterized by dipolarization of the geomagnetic

Table 1.2: Typical densities and ion temperatures (electron temperatures are generally slightly lower than ion temperatures) in some of the magnetospheric particle populations. (Partly from Egeland *et al.* [1996].)

Population	Number density n (cm^3)	Ion temperature $T_i(K)$
Magnetosheath	10^1	10^6
Plasma mantle	1	10^6
Tail lobe	10^{-2}	10^6
Plasma-sheet boundary layer	10^{-1}	10^7
Plasma sheet	10^0	5×10^7
Plasmasphere	10^3	10^{3-4}
Ionosphere	10^{1-6}	10^{3-4}

field. Simultaneously energization and injection of particles into the inner magnetosphere take place, as will be discussed in section 1.4.3. The substorms are regional compared to magnetic storms, usually appearing inside the auroral zone and lasting for two to three hours. Several substorms can be seen during one night.

1.4.2 Geomagnetic indices

Variations in the geomagnetic field are measured by geomagnetic observatories at various locations on the Earth. From these measurements a number of geomagnetic indices are computed [Mayard, 1980]. Only those relevant for the work of this thesis are described here.

The K-index is based on irregular variations in the geomagnetic H or D components (the horizontal component and declination) at each observatory. After the regular daily variation is removed, the difference between the highest and lowest values of these variations during a three hour interval is rescaled to a K-value of from 0 to 9. The K_p-index is defined as the weighed average of K-values from 13 selected geomagnetic observatories at sub-auroral latitudes. A low K_p-index indicates quiet geomagnetic conditions of the entire auroral zone, while a high K_p-index indicates disturbed conditions.

The AE-index ("auroral electrojet index") is calculated based on deviations in the H-components relative to a reference level at geomagnetic observatories inside the auroral zone. It is defined as the difference between the lowest (negative) value (the AL-index) and the highest (positive) value (the AU-index) of these deviations ($AE = AU - AL$), and is computed for 1-2 minutes intervals. Large changes in the AE-index are usually indications of substorms.

Another frequently used geomagnetic index is the D_{st}-index ("Disturbance storm time index"). It is obtained from H-component disturbances in the geomagnetic observatories near the geomagnetic equator where the magnetic perturbations are dominated mainly by the ring current. A large negative perturbation indicates an increase in the intensity of the ring current and is identified as a magnetic storm. The D_{st}-index is calculated on hourly basis.

Geomagnetic indexes thus provide an overview of the geomagnetic disturbance level during a given time period. They are widely used to identify magnetic storms/substorms.

1.4.3 Sources of magnetospheric plasma

There are two different ultimate sources for the particles in the magnetosphere; they can originate from the ionosphere or from the solar wind. The entering mechanisms and paths are numerous and a large part of them are still under investigation [Hultqvist *et al.*, 1999]. The particles may gain or lose energy or may change other properties (like pitch angles) during their path through interaction with waves or other particles. These particle properties in a given region at a given time might therefore provide a clue to identifying both the source and history of these particles.

The particles in a certain region of space can have several sources, and their trajectories are generally different if the particle energies are different. To discuss all possible entering mechanisms and paths is therefore outside the scope of this thesis. The following section will concentrate on the source of sub-keV ions in the sub-auroral region.

The sub-auroral region of the magnetosphere is generally known to be less dynamic than the auroral region, i.e. the temporal variations in the sub-auroral region are not as frequent as those in the auroral region (in both ions and electrons). The main reason for this low activity is believed to be that the sub-auroral region is not connected either to the interplanetary magnetic field (IMF) or the magnetotail. The ion clouds discussed in this thesis (Paper V) form an example of a temporal/spatial ion distribution in the sub-auroral region.

Although the following discussion concentrates on the source mechanisms for sub-keV ions in the sub-auroral region, these mechanisms may also apply to other energy ranges.

Upwelling ions from the ionosphere

Ionospheric ions might be accelerated upward and flow into the magnetosphere under the influence of plasma waves or potential drops parallel to the magnetic field, or a combination of the two. In case of a potential drop, the electrons are accelerated downward to cause electron precipitation.

Some of the upward flowing ions are completely lost to the open field lines or to the magnetotail, some return to the ionosphere on the same hemisphere at a slightly different latitude due to drift and possible acceleration in the magnetosphere, and some may travel along the magnetic field to the ionosphere on the conjugate hemisphere [Winningham *et al.*, 1984]. In the latter case the ions will undergo particle drifts and they will be observed as energy-time dispersed ion precipitation in the CPS region on the conjugate hemisphere. A possible conjugate electron precipitation (inverted V) will be observed in the BPS (Boundary Plasma Sheet) region.

Substorm injection from nightside magnetosphere

Geosynchronous satellites observes dipolarization of the geomagnetic field around the onset of substorms. This dipolarization is characterized by a sudden decrease in the V component (B_x) and an increase in the H component (B_z), and also dispersion-less Earthward energetic particle injections into the inner magnetosphere. This injection also accompanies by a sub-keV plasma injection. These injected particles will undergo particle drift and they show an energy-time dispersion when observed by low altitude satellites.

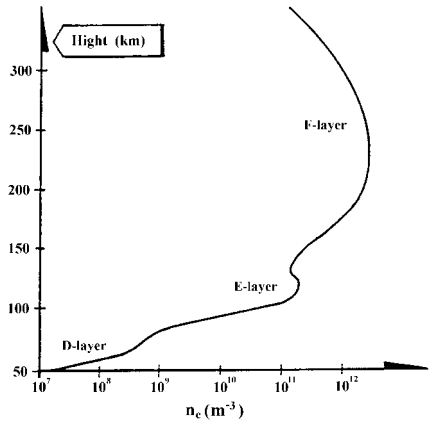

Figure 1.3: Electron density profile of the ionosphere during daytime. (Figure from Egeland *et al.* [1996].)

Solar wind direct injection

Solar wind plasma might also enter the ionosphere through the magnetopause or the high-altitude cusp to form the ionospheric LLBL (low latitude boundary layer), cusp, mantle, local injection signatures etc. Many mechanisms have been proposed [Hultqvist *et al.*, 1999, Ch. 5, 7]. These include merging/reconnection, diffusion, Kelvin Helmholtz instability, finite Larmor radius effects, indentation, weak magnetic field, Alfvén turbulence, and/or impulsive penetration.

1.5 Particle precipitation regions in the topside ionosphere

The region of plasma that is closest to the Earth is the ionosphere, and it is traditionally defined as the part of the atmosphere where the concentration of free electrons is high enough to influence radio wave propagation. Figure 1.3 shows the daytime electron density profile. The ionosphere is surrounded by the magnetosphere on its top-side (~500–1000 km height) and by the neutral atmosphere on its bottom-side (~80 km height). Ionospheric plasma is produced from ionization of thermospheric-molecules by solar radiation.

The ionosphere can be divided into horizontal layers (from low to high; D, E and F layers) with different ion composition and density (electron density is shown in Figure 1.3). We will in the following concentrate on the uppermost part of the ionosphere.

Figure 1.4 indicates the particle regions in the topside polar ionosphere [Newell and Meng, 1992; Lundin, 1997], based on in-situ particle measurements. The mapping relation between the ionosphere and the magnetosphere is still under debate and will not be discussed in detail here.

CPS and BPS are defined from in-situ electron measurements. Both CPS and BPS were originally believed to be the mapping of the Plasma Sheet into the ionosphere, and hence named Central Plasma Sheet (CPS) and Boundary Plasma Sheet (BPS) [Winningham *et al.*, 1975], but they have since then been re-defined following the morphology of observations. BPS corresponds to discrete auroral electron precipitation (structured electrons) that extends from the nightside into the dayside, while CPS corresponds to diffuse electron precipitation that is

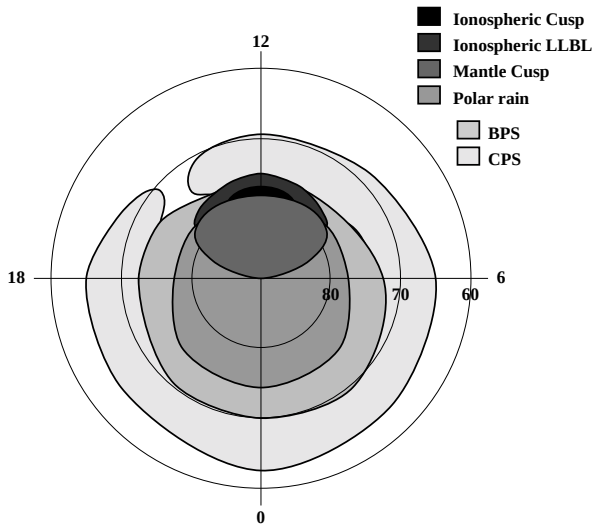

Figure 1.4: Particle precipitation regions in the polar upper ionosphere. Based ion and electron morphology as reported by Newell and Meng [1994], Feldstein and Galperin [1985] and Lundin [1997] during moderate K_p and southward IMF.

believed to be related to diffuse aurora. The CPS region is equatorward of the BPS region, but they might also overlap.

It should be noted that Figure 1.4 shows the average picture during weakly southward IMF and the reality is more dynamic. The general feature is that the regions expand equatorward for high K_p-index and larger southward IMF component. The high-latitude morphology drastically changes for northward IMF.

On the dayside the continuation of BPS-like electrons normally contains magnetosheath-like ions ($\sim$ 1 keV). This region is believed to be a mapping of the low-latitude boundary layer (LLBL) into the ionosphere.

Near noon, poleward of the ionospheric LLBL, is the ionospheric cusp. The cusp is the area of comparatively direct entry of plasma from the magnetosheath. The ion and electron distributions in the core part of the cusp have a fairly low temperature (<100 eV).

Poleward of the cusp is a region of reflected ions. The energy of ions in this region decreases with increasing latitude (velocity filter). This region is called the mantle cusp and it shrinks during northward IMF.

The polar cap is a nearly "empty" region surrounded by the Mantle and BPS. It contains a particle population called the polar rain. The polar rain consists of fairly Maxwellian and unstructured electrons usually around 100 eV with a little or no ion precipitation. The polar rain becomes intense, energetic and structured during northward IMF, and we then call it "polar shower".

1.6 Waves in plasmas

Any periodic motion of a plasma can be expressed as a superposition of sinusoidal oscillations with different frequencies, ω, and wavelengths, λ. Small amplitude oscillations can often be

expressed by one sinusoidal component:

$$A = A_0 e^{i(\mathbf{k}\cdot\mathbf{r}-\omega t)}, \tag{1.12}$$

where $\mathbf{k}$ is the wave vector (the wavelength is $\lambda = \frac{2\pi}{k}$), A_0 is the maximum amplitude, and $\mathbf{r}$ and t are the position and time. It can be shown that a point of constant phase of this wave will move with the phase velocity defined by:

$$v_p = \frac{\omega}{k}. \tag{1.13}$$

An infinitely long wave train with constant amplitude does not carry information. The wave has to be modulated to transmit information, which travels with the group velocity and not with the phase velocity. The group velocity is the velocity of the modulation of a wave and it is defined by

$$v_g = \frac{d\omega}{dk}. \tag{1.14}$$

For small amplitude oscillations the basic equations describing the wave or plasma dynamics can be linearized. This is done by separation of the variable into two parts, an equilibrium part, $\mathbf{A}_0$, and a perturbation part, $\mathbf{A}_1$ so that $\mathbf{A} = \mathbf{A}_0 + \mathbf{A}_1$, where only $\mathbf{A}_1$ is oscillating.

In a plasma where the electrons are displaced from the background ions, an electric field will build up, pulling the electrons towards neutrality, i.e. to their original position. The electrons will then overshoot because of their inertia and they will oscillate around the equilibrium position with a characteristic frequency known as the plasma frequency, ω_p. It is given by:

$$\omega_p = \sqrt{\frac{n_0 e^2}{\epsilon_0 m}}, \tag{1.15}$$

where n_0 is the plasma density, e is the elementary charge, ϵ_0 is the permittivity in vacuum, and m is the electron mass. Also low frequency waves can be excited in plasmas and in these cases both ions and electrons participate in the oscillations.

The plasma media supports a wide class of wave phenomena, but it is beyond the scope of this short introduction to summarize them all here. Therefore, only some examples of low frequency waves, these that are relevant for this thesis, will be described in the following.

1.6.1 Low frequency waves in a magnetized plasma

The linearized fluid equation of motion for ions or electrons in a magnetized plasma is given by

$$mn_0 \frac{\partial \mathbf{u}_1}{\partial t} = qn_0(\mathbf{E}_1 + \mathbf{u}_1 \times \mathbf{B}_0) - \gamma T \nabla n_1, \tag{1.16}$$

where m can denote the ion or the electron mass, respectively, u_1 is the appropriate fluid velocity, q is the particle charge, E_1 is the electric field perturbation, $\mathbf{B}_0 = B_0\hat{z}$ is the background magnetic field, $\gamma = C_p/C_V$ is the ratio of specific heats taken at constant pressure and constant volume, respectively, assuming adiabatic particle dynamics, T is the temperature, and n_1 is the density perturbation. The fluid velocities of the different species in the plasma can be combined to form an electric current defined by

$$\mathbf{j}_1 = \sum n_0 q \mathbf{u}_1 = \underline{\sigma} \cdot \mathbf{E}_1, \tag{1.17}$$

where the sum is over all species and $\underline{\sigma}$ is a complex, frequency-dependent electrical conductivity tensor. By inserting $\mathbf{j}_1$ into the wave equation (which is a combination of Amphère's law and Faraday's law),

$$k^2\mathbf{E}_1 - \mathbf{k}(\mathbf{k}\cdot\mathbf{E}_1) = \frac{\omega^2}{c^2}[\mathbf{E}_1 + i\frac{\mathbf{j}_1}{\epsilon_0\omega}], \tag{1.18}$$

we get

$$k^2\mathbf{E}_1 - \mathbf{k}(\mathbf{k}\cdot\mathbf{E}_1) = \omega^2\mu_0\underline{\epsilon}\cdot\mathbf{E}_1, \tag{1.19}$$

where $\underline{I}$ is the unit matrix, $\underline{\epsilon} = \epsilon_0(\underline{I} + i\underline{\sigma}/\epsilon_0\omega)$ is the dielectric tensor, and ϵ_0 and μ_0 are the permittivity and permeability in free space. By introducing the tensor $\mathbf{X} = \underline{I} - \mathbf{kk}/k^2$ into Eq. 1.19 we obtain

$$(\omega^2\mu_0\underline{\epsilon} - k^2\mathbf{X})\cdot\mathbf{E}_1 = 0. \tag{1.20}$$

For simplicity we take the $\mathbf{k}$-vector to have components only in the x and z directions, which does not limit the generality of the solutions. We then have $\mathbf{k} = k\sin\theta\hat{x} + k\cos\theta\hat{z}$, where θ is the angle between $\mathbf{k}$ and $\mathbf{B}$, which gives

$$\mathbf{X} = \begin{bmatrix} \cos^2\theta & 0 & \sin\theta\cos\theta \\ 0 & 1 & 0 \\ \sin\theta\cos\theta & 0 & \sin^2\theta \end{bmatrix} \tag{1.21}$$

The dispersion relation, $\omega = \omega(k)$, is then derived from the requirement of Eq. 1.20. For a nonzero $\mathbf{E}_1$ solution the determinant of the tensor quantity in the parenthesis of Eq. 1.20 must be zero, where $\underline{\sigma}$, and hence $\underline{\epsilon}$, is derived from Eq. 1.16 and 1.17.

In the cold plasma limit[2], $T_i = T_e = 0$ in 1.16 and we have

$$\underline{\epsilon} = \epsilon_0 \begin{bmatrix} \frac{1}{2}(R+L) & -i\frac{1}{2}(R-L) & 0 \\ i\frac{1}{2}(R-L) & \frac{1}{2}(R+L) & 0 \\ 0 & 0 & P \end{bmatrix}, \tag{1.22}$$

where

$$R \equiv 1 - \sum_j \frac{\omega_{pj}^2}{\omega}\left(\frac{\omega}{\omega \pm \omega_{cj}}\right), \tag{1.23}$$

$$L \equiv 1 - \sum_j \frac{\omega_{pj}^2}{\omega}\left(\frac{\omega}{\omega \mp \omega_{cj}}\right), \tag{1.24}$$

$$P \equiv 1 - \sum_j \frac{\omega_{pj}^2}{\omega}, \tag{1.25}$$

and ω_{pj} and ω_{cj} are the plasma and cyclotron frequencies for the different species, j. The dispersion relation for these waves can in this limit be solved in a rather easy way, giving rise to shear Alfvén waves and magnetosonic waves.

[2]This limit, in reality, assumes that the phase velocity of the waves is much larger than any thermal velocity of the species constituting the plasma. Thus, typically at resonances we expect thermal effects to be important.

1.6.2 Shear Alfvén waves

The shear Alfvén waves are a particularly important type of low frequency electromagnetic waves that propagate along the magnetic field. The dispersion relation for these waves can be found with $\theta = 0$. Under the assumption $\omega \lesssim \Omega_c \ll \omega_c$, we then obtain the following dispersion relation:

$$\tilde{n}^2 = \frac{c^2 k^2}{\omega^2} = 1 + \frac{\Omega_p^2 \Omega_c \mp \Omega_p^2 \omega}{\Omega_c(\Omega_c^2 - \omega^2)}, \tag{1.26}$$

where + and − give the right-hand (R-wave) and left-hand (L-wave) polarized waves, respectively, $\tilde{n}$ is the refraction index, and Ω_p and Ω_c are, respectively, the ion plasma frequency and ion cyclotron frequency, and ω_c is the electron cyclotron frequency. For low frequencies, the phase velocity of both modes can be written as

$$v_p = \frac{c}{\sqrt{1 + c^2/v_A^2}}, \tag{1.27}$$

where v_A is the Alfvén velocity defined as

$$v_A \equiv \frac{c\Omega_c}{\Omega_p} = \frac{B}{\sqrt{\mu_0 n M}}. \tag{1.28}$$

Taking $v_A \ll c$ in Eq. 1.27, we have $v_p \approx v_A$.

In the lowest frequency range of these waves ($\omega \ll \Omega_c$) both ions and electrons will have an $\mathbf{E}_1 \times \mathbf{B}_0$-drift and the ions will in addition have a low frequency polarization drift which is small compared to the $\mathbf{E}_1 \times \mathbf{B}_0$-drift. The magnetic field lines in an Alfvén wave "move" with the same velocity, $\mathbf{v}_\perp = \mathbf{E}_1 \times \mathbf{B}_0/B^2$. The plasma thus acts as if the particles were frozen to the field. Strictly speaking, it is not possible to identify the motion of a magnetic field line, and the "frozen-in" field line concept states in reality only that *within the applicability of Magneto Hydrodynamics (MHD)* we are not making any errors by *assuming* magnetic field lines to follow the particle motion.

From Faraday's law ($\nabla \times \mathbf{E}_1 = -\frac{\partial \mathbf{B}_1}{\partial t}$) the fluctuating wave magnetic field is given by

$$E_x = \frac{\omega}{k} B_y. \tag{1.29}$$

By combining Eq. 1.29 and 1.28 we see that the E_x/B_y-ratio for an Alfvén wave will be equal to the Alfvén velocity, v_A, in the low frequency range.

1.6.3 Magnetosonic waves

If we then consider low-frequency waves that propagate in the direction perpendicular to $\mathbf{B}_0$ we find the magnetosonic wave. For this case we will have $\theta = \pi/2$ and the dispersion relation is given by

$$\tilde{n}^2 \left(\frac{\Omega_c^2 - \omega^2 + \Omega_p^2}{\Omega_c^2 - \omega^2} + \frac{\omega_p^2}{\omega_c^2} \right) = \left(\frac{\Omega_c^2 - \omega^2 + \Omega_p^2}{\Omega_c^2 - \omega^2} + \frac{\omega_p^2}{\omega_c^2} \right)^2 - \left(\frac{\Omega_p^2 \omega}{\Omega_c(\Omega_c^2 - \omega^2)} \right)^2, \tag{1.30}$$

where ω_p is electron plasma frequency.

In general the cold plasma is frozen to the magnetic field for the lowest frequencies ($\omega \ll \Omega_c$). Note that the major difference between the shear Alfvén wave and the magnetosonic wave is

that the latter has a finite value for $\mathbf{k}\cdot\mathbf{u}_1$. As this wave propagates across the magnetic field it compresses and expands the plasma alternately together with the "frozen-in" magnetic field lines. This acts like a sound wave and hence the wave is called the magnetosonic wave. The phase velocity of the magnetosonic wave will also be equal to the Alfvén velocity in this low frequency, cold plasma limit. In a warm plasma (finite pressure) the phase velocity of the magnetosonic wave will increase (Eq. 1.30 will contain the sound speed) so that $\omega/k > v_A$.

The Lower hybrid wave

For resonance ($k \to \infty$ and thus also $\tilde{n} \to \infty$) of the magnetosonic wave the term in brackets on the left-hand side of Eq. 1.30 must go to zero. The dispersion relation for this resonance is given by

$$\omega^2 = \frac{\omega_p^2\Omega_c^2 + \omega_c^2\Omega_c^2 + \omega_c^2\Omega_p^2}{\omega_p^2 + \omega_c^2} \approx \frac{\omega_c\Omega_c(\Omega_c^2 + \Omega_p^2)}{\Omega_p^2 + \Omega_c\omega_c} = \omega_{LH}^2. \tag{1.31}$$

In this limit the wave is called the lower hybrid wave and ω_{LH} is the lower hybrid frequency.

In a thermal plasma the frequency does not reach an asymptotic value for high k-values and the approximate dispersion relation for this wave is then found to be (following Shapiro *et al.* [1993])

$$\omega = \omega_{LH}\left(1 + \frac{1}{2}(kR)^2 + \frac{1}{2}\frac{M}{m}\left(\frac{k_{||}}{k}\right)^2 - \frac{1}{2}\frac{\omega_p^2}{(kc)^2}\frac{\omega_p^2}{\omega_p + \omega_c}\right), \tag{1.32}$$

where $k_{||}$ is the wave-number parallel to $\mathbf{B}_0$, m and M are the electron and ion masses, c is the speed of light, and R is the dispersion length given by

$$R^2 = \left(3\frac{T_i}{\omega_{LH}^2 M} + 2\frac{T_e}{\omega_c^2 m}\frac{\omega_p^2}{\omega_p^2 + \omega_c^2}\right). \tag{1.33}$$

This dispersion relation is derived from the assumption that, to the lowest order in ω, the lower hybrid wave dispersion relation is $\omega^2 = \omega_{LH}^2$, i.e. purely electrostatic. This simple estimate is then expanded by corrections due to finite temperature and the lowest order correction from electromagnetic effects to give the result in Eq. 1.32 and 1.33. This dispersion relation bends upward for high k-values (due to finite temperature) and downward for low k-values (due to electromagnetic effects). The result of Eq. 1.32 and 1.33 will be less correct for low k than the result from Eq. 1.30 since only the lowest order of electromagnetic effects is included. The full dispersion relation for magnetosonic waves and lower hybrid waves is shown in Appendix A.

1.6.4 Classification of waves

To be able to distinguish and identify the different types of waves in a plasma we usually use the following characteristics

- frequency
- wavelength (usually not that easily obtained from satellite data)
- electrostatic ($E/B \to \infty$) / electromagnetic (finite E/B) / magnetostatic ($E/B \to 0$)
- propagation angle to $\mathbf{B}_0$

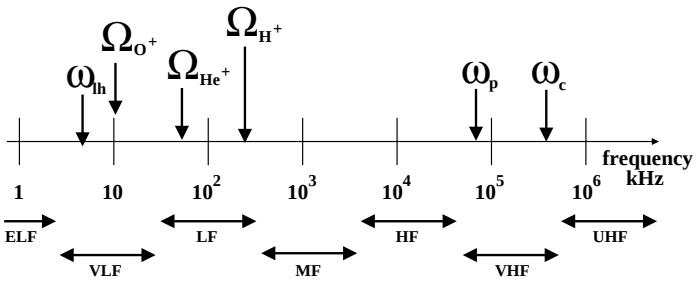

Figure 1.5: Relative frequency scales (on logarithmic axis) of the lower hybrid frequency (ω_{lh}), the electron plasma-frequency (ω_p), the electron cyclotron-frequency (ω_c) and the ion cyclotron-frequencies (Ω_{H^+}, Ω_{He^+}, Ω_{O^+}) in the auroral/sub-auroral zone at $\sim$ 1700 km. (Based on numbers from Paper II of this thesis.)

The properties that are most easily obtained from satellite measurements are the frequency and the E/B-ratio. Figure 1.5 roughly illustrates relative values of the lower hybrid frequency, the electron plasma-frequency, and the ion and electron cyclotron frequencies in the sub-auroral zone at $\sim$ 1700 km.

We note that the shear Alfvén waves and the magnetosonic waves are electromagnetic while lower hybrid waves are mainly electrostatic. We also recall from the previous discussion that Alfvén waves will have an E/B-ratio equal to the Alfvén velocity. This is widely used as an identification criterion for Alfvén waves.

1.7 Nonlinear effects

A large amplitude wave can exert a wave pressure force on the background plasma. This force is called the *ponderomotive force* and can be generated in a spatially inhomogeneous wave. The wave interacts nonlinearly with the background plasma through the ponderomotive force. This may in turn change the propagation properties of the wave itself, affect the propagation of other waves, or even lead to interaction between different waves. As a result this might create or enhance a strongly inhomogeneous plasma state. One example of such an inhomogeneous plasma state is a plasma which contains a large number of randomly distributed cavitons, i.e. wave-filled density cavities. These cavitons may under some conditions (when the threshold for the modulational instability is reached) evolve into a collapsing state where they become narrower, the density decreases and the wave amplitude increases with time. This collapse will continue until burnout sets in.

Collapse of Langmuir waves [Zakharov, 1972] is well known and studied theoretically, numerically as well as by controlled laboratory experiments. There are also several other types of waves that can give cavity formation and collapse. Some of these are kinetic Alfvén waves, magnetosonic waves and lower hybrid waves. A collapse theory of lower hybrid waves will be briefly discussed below (following Treumann and Baumjohann [1997] and Robinson [1998]). The lower hybrid collapse is not as well understood as the Langmuir collapse, although some numerical studies have been carried out. It is important to note, however, that even though the wave collapse cannot be doubted as a physical reality, it still remains an open question to what extent it is a spontaneously occurring phenomenon in nature, and if so, whether it is important for the overall plasma dynamics.

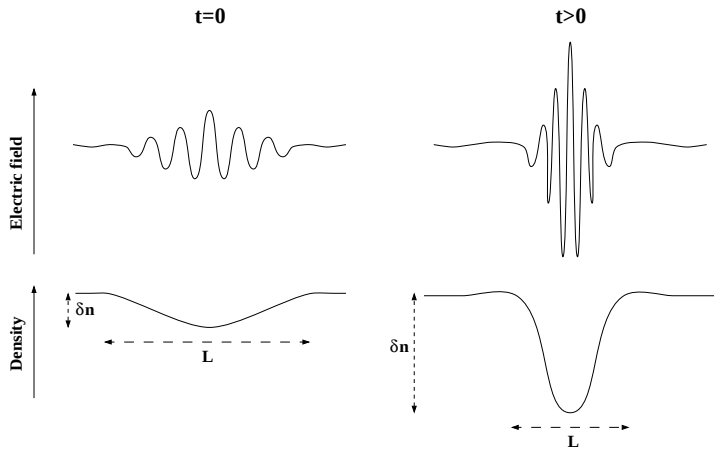

Figure 1.6: Sketch of the evolution of density cavities during collapse.

1.7.1 Lower hybrid turbulence

The nucleation cycle is one of the main features of certain types of strong plasma turbulence where many interacting degrees of freedom for the plasma dynamics are excited simultaneously. This cycle includes nucleation, collapse, burnout, and relaxation. We will here discuss the nucleation cycle of lower hybrid turbulence, but other waves may experience a similar fate, as previously mentioned.

Trapped (localized) waves can nucleate energy from propagating (delocalized) waves. The nucleation is most effective when the frequency of the trapped wave is close to the lower hybrid frequency. The trapped wave continues gaining energy until the modulational instability threshold is reached and collapse sets in. During the collapse phase the density perturbations become large, so that the frequency of the trapped eigenmodes increases away from those of the propagating modes, and hence the energy transfer between the modes will decrease. Figure 1.6 shows the evolution of a localized wave and caviton during collapse. When the collapsing cavitons have become so narrow that the phase velocity of the trapped wave matches the thermal velocity of the plasma, the trapped waves will become damped through wave-particle interactions (often modeled by linear Landau damping, but this is questioned since the waves are strongly non-linear). This is the burnout phase and it may result in particle acceleration and localized heating. After this burnout, the empty density wells relax back toward the original nucleation scale since they are no longer supported by the wave. When the frequency of the localized modes reaches the frequency of the propagating waves, the nucleation again takes place and the cycle continues.

The threshold value for modulation instability and caviton formation by lower hybrid waves is generally low enough to easily reach that threshold value. Once this threshold is exceeded, the waves will undergo modulation instability, cavity formation, and collapse.

The collapse of lower hybrid waves in the purely electrostatic limit obeys the following equation:

$$\left(\frac{\partial^2}{\partial t^2} - c_{ia}\nabla^2\right)\delta n = \frac{i\epsilon_0}{4M}\frac{\omega_p^2}{\omega_c\omega_{LH}}\nabla^2(\nabla\delta\phi^* \times \nabla\delta\phi)_{||}, \tag{1.34}$$

where c_{ia} is the ion acoustic speed, δn is the density variation forced by the wave, and $\delta\phi$ and $\delta\phi^*$ are the electric wave potential and its complex conjugate. The right hand side of

Eq. 1.34 represents the ponderomotive force by the lower hybrid wave pressure. Eq. 1.34 enables a rough estimate of the relation between density depletion and energy density of the wave electric field, W_E, during the collapse phase for the subsonic case (i.e. when the second term exceeds the first term on the left hand side of Eq. 1.34):

$$\delta n \propto W_E. \tag{1.35}$$

During collapse the density usually evolves as

$$\delta n \propto \frac{1}{t_c - t}, \tag{1.36}$$

where t_c is the constant time when the collapse ends (this time, t_c, will never be reached in practice). The energy density of the wave in Eq. 1.35 will therefore also increase with time. The evolution of density cavities during collapse is sketched in Figure 1.6.

The cavitons resulting from lower hybrid wave collapse are expected to have two-dimensional structures that form cigars with transverse and parallel lengths (relative to the magnetic field) given by

$$L_\perp \approx R\sqrt{\frac{\alpha m}{2M}\frac{n_0 k_B (T_e + T_i)}{W_{lh}}} \tag{1.37}$$

$$L_\parallel \approx \frac{L_\perp^2}{R}\sqrt{\frac{M}{m}}, \tag{1.38}$$

where $\alpha = (1 + \omega_c^2/\omega_p^2)^{-1}$, k_B is the Boltzmann constant, R is defined in Eq. 1.33, T_e and T_i are the electron and ion temperatures, and W_{lh} is the energy density of the lower hybrid waves. These cavitons are elongated along the magnetic field and propagate at the ion-acoustic velocity across the magnetic field lines. The length scales will, during collapse, evolve as

$$L_\parallel \propto 1 - t/t_c \propto L_\perp^2, \tag{1.39}$$

according to Kuznetsov and Skoric [1988].

Several studies have tried to explain the lower hybrid cavity observations in the Earth's upper ionosphere (such as the ones in this thesis, Paper I, II, III and Appendix A) as caused by the collapse of lower hybrid waves (e.g. Robinson [1998]). The observations presented herein do not, however, seem to agree with the collapse theory. In these data, the deepest cavities (largest δn) are generally the widest ones (largest $L_\perp$) and the shallowest ones are generally the narrowest ones, and are thus not in agreement with Eq. 1.36 and 1.39.

1.8 Density cavities in space plasma

Different types of cavities are observed in the upper ionosphere, ranging from a few tens of meters up to several hundreds of kilometers in length scale perpendicular to the magnetic field. The cavities are usually grouped into four categories; large scale ($\sim$ 1000 km) as reported by e.g. Benson and Calvert [1979], medium scale ($\sim$ 1 - 50 km) as reported by e.g. Johnson and Chang [1995], small scale ($\sim$ 500 m) as reported by e.g. Wahlund *et al.* [1994], and tiny scale ($\sim$ 50 m) as reported by e.g. LaBelle *et al.* [1986]. These cavities have different generating mechanisms and are correlated with various degrees of heating of ions and electrons, as indicated in Table 1.3.

The *Auroral Density Cavity* (ADC) and the *Low Latitude Cavity* (LLC) are large scale density cavities (see Section 1.8.2). The ADC is a region over the auroral zone and polar cap with diminished plasma density. It contains ion heating and is associated with the source of auroral kilometric radiation [Calvert, 1981]. The LLC is a region of density depletion equatorward of the auroral oval. This cavity is believed to be the projection of the plasmapause onto the ionosphere, and is frequently referred to as the mid-latitude trough [Muldrew, 1965].

Medium scale cavities are associated with large, radially divergent intense electric fields and fine scale *black auroral structures*, either east-west aligned dark striations or black auroral curls. These electric fields are correlated with dropouts in electron precipitation and intense precipitating or transversal ion fluxes [Marklund *et al.*, 1997].

Alfvén waves might be trapped in plasma cavities (small scale cavities). These waves then form standing resonant modes in the perpendicular direction (to the magnetic field). The *Alfvén solitary structures* are associated with some field-aligned currents [Stasiewicz *et al.*, 1997].

Lower hybrid cavities, or tiny scale cavities, are associated with lower hybrid waves (see Section 1.8.1). They are identified by a density depletion of a few percent that appears simultaneously with an enhancement in lower hybrid wave amplitude up to 100 mV/m.

The scale sizes for these different types of cavities are given in Table 1.3 for an altitude around 1700 km. It has to be noted that these scale sizes (perpendicular to the magnetic field) also depend on the altitude of observation because of the projection along the magnetic field. Charged particles can move large distances along the magnetic field lines compared to movement across the magnetic field lines. A density depletion (cavity) will thus be projected along the magnetic field lines. As a result the width (scale size) of the depleted area grows with increasing altitude. The scale sizes given in Table 1.3 correspond to an altitude around 1700 km.

1.8.1 Lower hybrid cavities

Lower hybrid cavities (LHCs), also called Lower Hybrid Solitary Structures (LHSS), have been detected in the ionosphere by the sounding rockets Marie [LaBelle *et al.*, 1986], Topaz II and III [Vago *et al.*, 1992], Amicist [Lynch *et al.*, 1996], Phaze II [McAdams *et al.*, 1998], and Oedipus-C [Knudsen *et al.*, 1999], and also by the Freja satellite [Dovner *et al.*, 1994; Eriksson *et al.*, 1994; Dovner *et al.*, 1997; Pécseli *et al.*, 1996, and Paper I, II, III of this thesis].

These cavities are of strong interest for the auroral plasma physics community, because coherent and solitary structures are believed to play an important role in energy transfer between particles and waves and also between waves. LHCs are mainly studied from the

Table 1.3: Different types of density cavities in the ionosphere (AKR = Auroral Kilometric Radiation). The scale sizes are taken at an altitude of about 1700 km.

Type	**scale size $\perp$ B**	**Correlated with**	
Large scale cavities, ADC	$\sim$ 1000 km	AKR + inv. V's	ion + electron heating
Large scale cavities, LLC	$\sim$ 500 - 1000 km	proj. plasmapause	(weak ion heating?)
Medium scale cavities	$\sim$ 1-50 km	"black aurora"	mainly ion heating
Small scale cavities	$\sim$ 500 m	Alfvén waves	mainly ion heating
Tiny scale cavities	$\sim$ 50 m	Lower hybrid waves	(weak ion heating?)

basic plasma physic point of view, i.e. the space plasma is used as a plasma laboratory.

The characteristic feature of these cavities is a density depletion accompanied by an enhancement of the electric field fluctuations around the lower hybrid frequency, giving the appearance of wave-filled cavities. Ray-tracing of lower hybrid waves [Pécseli *et al.*, 1996] indicates that these waves will spend more time inside a density cavity than outside, resulting in wave amplitude enhancement. The scale size of these cavities ($\sim$ 50 m) is compatible to or larger than a typical ion Larmor radius, and this indicates that if ions are heated by the wave they might escape mainly perpendicular to the magnetic field while possibly heated electrons escape mainly along the magnetic field. This is also confirmed by the shape of the cavities (Paper II): they have a cylindrically symmetric Gaussian shape. If all thermal ions that have their gyro-center on a selected magnetic field line are removed, the resulting density depletion will be a Gaussian.

Data from sounding rockets like Amicist show evident ion heating inside LHCs [e.g. Lynch *et al.*, 1999], but such heating has not been observed in the Freja satellite data. Although ion energization by lower hybrid waves is reported by André *et al.* [1994], they find no correlation with density cavities on Freja (LHCs). We note also that a study of data from the cold plasma analyzer on Freja [Knudsen *et al.*, 1998a] shows ion energization inside areas of LHCs but no clear correlation with individual LHCs is seen. This needs further investigation. A discussion of the sensitivity of the Freja hot ion experiment (TICS) is given in Appendix D.

Knudsen *et al.* [1999] reports on a study of two-point measurements by the Oedipus-C sounding rocket. This experiment consisted of two Langmuir probes on separate sub-payloads several hundred meters apart along the magnetic field at an altitude around 500 - 800 km. One conclusion from this study is that the cavities extend at least 800 m along the magnetic field and the parallel length of these cavities is currently believed to be several km.

A statistical study of satellite data (Paper I) find lower hybrid cavities mainly in the pre-noon sector. This is known to be an area with enhanced wave-particle interactions [Østgård *et al.*, 2000].

Paper I in this thesis finds that these cavities are Poisson-distributed in space, indicating a random formation process. This rules out, according to Pécseli *et al.* [1996], a interpretation that the observations are related to an early stage of a modulation instability (e.g. Musher and Sturman [1975], Retterer *et al.* [1986], or Shapiro *et al.* [1993]). Robinson [1998] reports that the full nucleation scenario for maintenance of strong turbulence (see section 1.7.1) might explain the LHCs. It is argued that the wave packets spend most of their time in the relaxation and nucleation phases, rather than undergoing collapse and burnout.

Another scenario described by Schuck *et al.* [1998] and Bonell *et al.* [1998] suggests that the cavities can be explained through interaction between lower hybrid waves and preexisting density depletions. In this scenario they consider the Hall current to be produced by $\mathbf{E} \times \mathbf{B}$ drifting electrons, while the ions do not drift because they are nearly unaffected by the magnetic field, on the time scale of interest. As a result, the lower hybrid waves inside cavities will rotate around the magnetic field. They also propose auroral hiss as a possible source of power for this process. The theory of linear scattering on preexisting density depletions is supported by data from the Phaze II sounding rocket [McAdams *et al.*, 1998], but they see solitary lower hybrid waves on steep gradients (positive or negative) of density fluctuation rather than inside cavities (localized depletions in density).

Laboratory experiments have shown that whistler waves incident on a field-aligned density striation may produce lower hybrid waves via a linear mode-coupling mechanism [Rosenberg and Gekelman, 1998, 2000]. Other generation mechanisms for lower hybrid waves involve

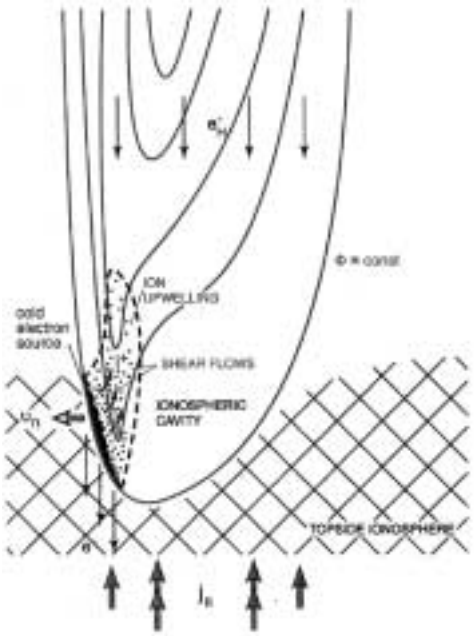

Figure 1.7: Sketch of the auroral density cavity (ADC) (from Haerendel [1999]).

Alfvén and/or fast magnetosonic waves [Khazanov *et al.*, 2000, 1997].

As outlined here the lower hybrid cavities have been a subject of intensive study both experimentally and theoretically, but there is still no concensus on the formation process of these density cavities and waves.

1.8.2 Large scale density cavities

There are at least two types of large scale density cavities, as mentioned above, the auroral density cavity (ADC) and the low latitude density cavity (LLC). They have approximately the same scale size, but are found in different locations and are the result of different mechanisms. Paper IV of this thesis gives a more detailed discussion of the ADCs and LLCs observed by the Astrid-2 satellite.

The auroral density cavity

The auroral density cavity (ADC) is located inside the auroral zone and has been observed by several satellites [e.g. Lundin and Hulqvist, 1989; Persoon *et al.*, 1998; Calvert, 1981, Paper IV of this thesis]. These cavities are accompanied by heated ions. Studies of possible acceleration mechanisms for these ions [Doe *et al.*, 1995; Rönnmark, 1999] have shown that upward field-aligned electric field might accelerate ions and result in the formation of large depletions in the background density. Figure 1.7 is a sketch of the ADC.

Auroral kilometric radiation (AKR) is also found to originate from local depletions of electron density, like ADCs [Benson and Calvert, 1979]. It can be argued that waves in a low density plasma will accelerate ions more easily than waves in a denser plasma. As a result the plasma density will become even lower, forming a feedback loop [Lysak, 1991].

Several studies of ADCs [Hamrin *et al.*, 2000; Klumpar, 1979; Norqvist *et al.*, 1998b; Collin

et al., 1998; Mäkelä *et al.*, 1998] indicate that the degree of density depletion inside ADCs depend on the ionospheric illumination. Both the background density and the density inside cavities are lower when the ionosphere is in darkness. This indicates that the ionospheric conductivity [Newell *et al.*, 1996, 1998] plays a role in the formation of ADCs. A clear correlation between the strength of energization of ions (energy of heated ions) and the depth of the density depletion is also found [Lundin *et al.*, 1994c; Hamrin *et al.*, 2000]. The deepest cavities contain ions with the highest energies.

The low latitude density cavity

The low latitude density cavity (LLC), which is probably related to the ionospheric trough, is a density depletion that exist at the projection of the plasmapause along geomagnetic field lines [Muldrew, 1965; Rycroft and Thomas, 1970; Thomas and Andrews, 1968; Akasofu and Chapman, 1972]. It is observed equatorward of the auroral oval, thus at lower latitudes than the ADC.

Several different explanations have been proposed for the association between the LLC and the plasmapause (see Rycroft and Thomas [1970]). Gulikov *et al.* [1990] discuss the "total shadow" phenomenon. Here the trough is seen as an area of less ionization between the solar radiation ionization on the equator-side and the auroral zone on the poleward side. However, a study of LLC by the Astrid-2 satellite [Paper IV of this thesis] indicates that they are mainly observed on the night-side, but during both polar summer and polar winter.

1.9 Freja and Astrid-2

The studies included in this thesis are based on data from the Freja and Astrid-2 satellites. The following is a brief overview of the operation of and experiments on board these satellites. For a more detailed description see Lundin *et al.* [1994a,b] and André [1993] for the Freja satellite, and Blomberg *et al.* [1997] for the Astrid-2 satellite.

1.9.1 The Freja satellite

Freja was launched on October 6th 1992, and orbited at 600-1750 km altitude with a velocity of 7 km/s and a spin period of 6 s. Its operational lifetime was 4 years. The satellite was like a spinning disk with a diameter of 2.2 m and a mass of 214 kg (in orbit). A view of Freja is shown in Figure 1.8. The axis of the disk pointed in the direction of the Sun so that the solar panels on the top of the satellite were illuminated. Data from the satellite were received at The Swedish Space Corporation's Esrange ground station in Kiruna, Sweden and at the Prince Albert satellite station in Canada. The high resolution of the instruments on board Freja enabled studies of small-scale phenomena of down to a few meters in scale length (e.g. the lower hybrid cavities).

The wave and plasma density experiment had a temporal resolution, τ, equivalent to a few meters in spatial resolution, l, (under $l \sim V \cdot \tau$, where V is the satellite velocity) in the medium frequency range (1 Hz - 16 kHz). It measured variations in the electric and magnetic fields, variation in the plasma density, and also the electron temperature and total plasma density. The electric field and density were measured by spherical Langmuir probes on wire-booms in the satellite spin plane. A sketch of the boom configuration is shown in Appendix C. The magnetic field was measured by a three-axis search-coil magnetometer.

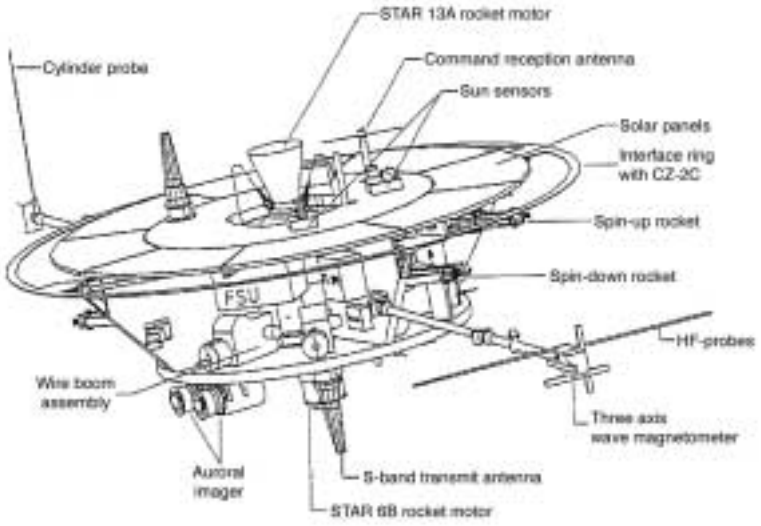

Figure 1.8: The Freja spacecraft (from Lundin *et al.* [1994b]). For a view of the wave experiment see Appendix C.

The hot plasma experiment measured the electron distributions in the energy range ≈ 0.1 -100 keV and positive ion distributions (with mass identification) in the energy range of $\approx$ 1 eV - 5 keV. The dwell time in the ion measurements on each energy level was 10 ms and 16 or 32 energy steps were used. This gave a temporal resolution of a few tens of meters for a full energy spectrum. The hot plasma experiment could also be used in a constant energy mode [Norqvist *et al.*, 1998a]. This enabled an even better temporal resolution for that particular energy. See also Appendix D for a discussion of the sensitivity of this instrument.

Other experiments on the Freja satellite measured the electrostatic and magnetic vector fields, the cold ion and electron distributions, and ultra-violet auroral images.

1.9.2 The Astrid-2 satellite

A much smaller satellite (micro-satellite), Astrid-2, was launched in December 1998 and was operational until July 1999. The spacecraft had a circular orbit with 83 degrees inclination and an altitude of 1000 km. The payload weight was less than 10 kg and it had a rectangular shape (45 cm $\times$ 45 cm $\times$ 30 cm) with solar panels folded out outside the main body. A view of the Astrid-2 satellite is shown in Figure 1.9. The satellite was spinning with a spin period of 8 s and spin axis pointing towards the sun. The data were received by the Swedish Space Corporation (SSC) in Stockholm (Solna) and at the South African base Sanae IV on the Antarctic continent.

The Astrid-2 scientific payload included four experiments: EMMA (electric and magnetic fields), LINDA (plasma density), MEDUSA (electron and ion spectrometer) and PIA (photometer):

- The EMMA electric field instrument measured E-field in the spin plane by means of four wire booms and the EMMA magnetometer was mounted on a stiff boom along the satellite spin axis pointing away from the sun.
- The plasma density was measured by the LINDA experiment that consisted of two

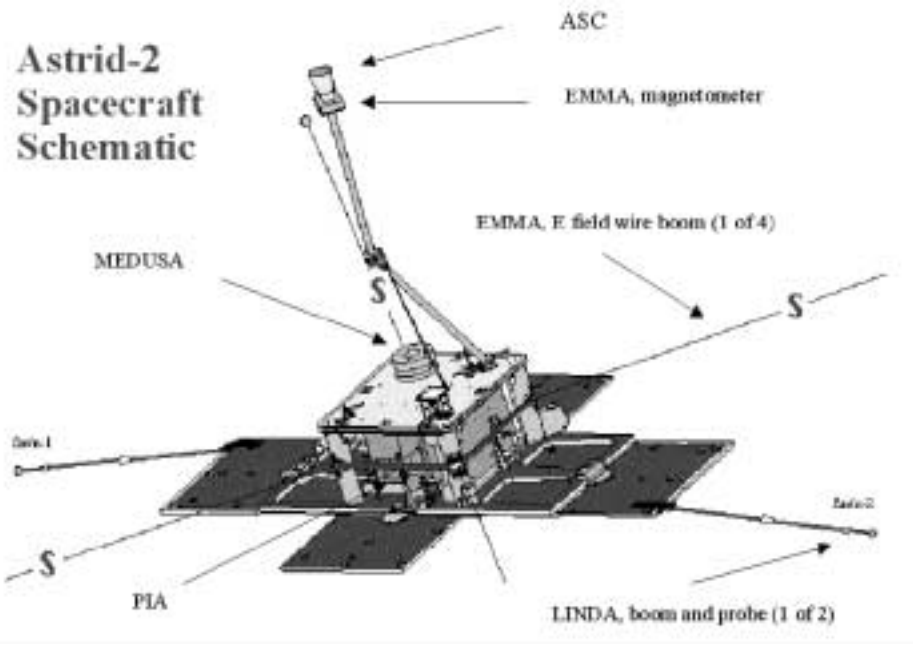

Figure 1.9: The Astrid-2 spacecraft and instruments (from Blomberg *et al.* [1997]).

Langmuir probes mounted on wire booms in the spin plane.

- MEDUSA was a combined electron and ion spectrometer. It measured electrons and ions at energies up to 18 keV/q simultaneously. The particles were measured in 16 sectors in a plane almost parallel to the spin plane and the temporal resolution was limited by 16 energy sweeps per seconds for electrons and 8 energy sweeps per second for ions.
- PIA consisted of three photometers, one pointing towards the sun and the two others mounted in the spin plane.

1.9.3 Similarities and differences between the two satellites

Both Freja and Astrid-2 were polar orbiting satellites, but Astrid-2 had a higher inclination (83°) than Freja (63°), whereas Freja had a higher altitude (around 1700 km near the auroral region) than Astrid-2 (1000 km). Freja was active during almost four years from 1992 to 1996 while Astrid-2 took data for half a year during the spring of 1999.

Both satellites were designed for auroral microstructure research. Freja had some additional instruments to those on Astrid-2, but otherwise most of the instruments had similar function. The wave instrument on Astrid-2 was a simplified version of that of Freja, and did not measure as high frequencies as the ones on Freja. It was therefore not possible to measure lower hybrid waves with Astrid-2. Astrid-2 did, on the other hand, measure plasma densities, electric fields, and magnetic fields over whole orbits as opposed to Freja where data were mainly taken at high latitudes.

Freja and Astrid-2 did similar measurements at different times and heights in the upper ionosphere and have together given us a large and interesting dataset that will continue to be analyzed for many years.

2
Summary of papers

This thesis presents different types of localized plasma phenomena. It concentrates on lower hybrid cavities (LHC), large scale cavities, and ion clouds. More than 50 % of the work in the papers presented in this thesis has been done by the first author.

Paper I "Statistics of Lower–Hybrid Wave Cavities Detected by the FREJA Satellite" describes the basic properties of lower-hybrid wave cavities. The paper provides a survey of the conditions for occurrence and spatial distribution of the cavities. It describes basic features of individual cavities, and associated fluctuating electric fields, and gives typical densities, widths, and other characteristics for selected orbits. The cavities are found to be Poisson-distributed in space with an average distance between cavities of approximately 350 m. Both a propagating wave (existing both inside and outside the cavity) and a localized wave (trapped) are found, and the latter has a frequency below that of the propagating component. The trapped component is observed in approximately 10% of the observed cavities.

Paper II "Cavitation of Lower–Hybrid Waves in the Earths Ionosphere; a model analysis" reports on the shape of individual cavities. It shows that a cylindrically symmetric Gaussian density depletion gives a very good fit for a vast majority of cases. Inversely, by assuming this shape for all cases, a number of well-defined characteristics are obtained, setting restrictions on the theory describing the observed wave phenomena. Methods for obtaining the velocity distribution of the cavities are also outlined.

Paper III "Lower Hybrid Waves in the Earths Upper Ionosphere - Wave Cavitation and Ion Heating" examines the spatial distribution of lower hybrid waves and cavities, and compares them against the energy-distribution of ions. The study indicates that formation of these cavities and ion energization are separated and unrelated events to each other at Freja altitudes (1700 km).

Paper IV "Statistical study of large-scale density cavities observed by ASTRID-2" presents a statistical study of large-scale density cavities: the Auroral Density Cavity (ADC) and the Low Latitude Density Cavity (LLC) observed by the Astrid-2 satellite. The results show that while both LLCs and ADCs occur most frequently on the night side, ADCs occur only in a non-illuminated ionosphere while LLCs also occur in an illuminated ionosphere. Both ADCs and LLCs are mainly seen during low to moderate K_p. For ADCs this indicates that the low altitude boundary of these cavities is generally above Astrid-2's altitude (1000 km) for higher K_p because: 1) these cavities show an even distribution of occurrence for all K_p above the lower altitude boundary, and 2) the altitude of this boundary is decreasing for decreasing K_p.

Paper V "Dense ion clouds of 0.1-2 keV ions inside the CPS-region during low K_p observed by Astrid-2" reports unusual observations of dense ion clouds in the 0.1-2 keV energy range by the Astrid-2 satellite. These ion clouds are found predominantly in the early morning sector, deep inside the "closed" magnetic field region. Three alternative explanations for these ion clouds are given: 1) they could have originating from substorm-related ion injections in the night side, 2) they could be signatures of direct solar wind injections, or 3) they could be a result of up-welling ions from the opposite hemisphere. None of these scenarios, however, account for all of the observed properties.

3
Conclusion/Future work

Statistical studies of lower hybrid cavities (LHCs) observed by the Freja satellite have shown that they are Poisson distributed in space and that the density depletions have a cylindrically symmetric Gaussian shape. These observations need to be embedded in future theoretical models for LHCs. The LHCs are also found to be stationary in the transversal time of Freja ($\sim$10 ms). They have a spatial width across the magnetic field of $\sim$ 50 m and an average density depletion of $\sim$ 2.1 %. A large number of LHCs are usually observed together and areas of LHCs along Freja's trajectory range from 10 km to 1500 km with an average distance between individual LHCs of 350 m.

The observations also show two different wave modes inside some of these cavities. These are interpreted as a propagating mode (at the highest frequency) and a trapped mode (at the lowest frequency). Both modes are found to be electrostatic. Low frequency electromagnetic waves are also observed in regions with lower hybrid cavities. These waves are most easily explained as magnetosonic waves.

Ion heating inside LHCs is not observed by the hot ion experiment (TICS) on Freja, as opposed to rocket measurements. This cannot be explained by the sensitivity limit of the instrument. Simulations of the TICS instrument show that LHC ion heating events like those observed by rockets should also have been observed by TICS if there were any. Therefore we believe the difference between the LHC observations by Freja and sounding rockets to be real. This needs further theoretical and experimental investigations.

Another issue that should be addressed in the future is the extent of LHCs parallel to the magnetic field. This could be done by multi-point measurements along the magnetic field similar to the study by Knudsen *et al.* [1999] but with a distance along the magnetic field of several km. Studies of waves, plasma density, and energy and pitch angle distribution of charged particles at different points along lower hybrid cavities might also help us explain the currently observed difference between satellite and rocket measurements. It would also be interesting to measure magnetic field, electric field, and plasma density on the scale of individual cavities so as to be able to investigate the electrostatic/electromagnetic nature of the lower hybrid and magnetosonic waves in more detail.

Auroral density cavities (ADCs) and low latitude density cavities (LLCs) observed by the Astrid-2 satellite show a scale size across the magnetic field of $\sim$ 500 – 1000 km. Both ADCs and LLCs are seen on the night-side, and ADCs are seen only in the non-illuminated ionosphere, i.e. during polar winter, while LLCs are seen also in the illuminated ionosphere. This difference comes from the fact that ADCs are a result of plasma outflow related to field-aligned currents while LLCs are probably related to a trough phenomenon. The lower altitude boundary of ADCs for moderate K_p is indicated to be close to the Astrid-2 altitude (1000 km) since the lower altitude boundary of ADCs is believed to move upward for high K_p and an equal probability of all K_ps is seen at higher altitudes. Future studies by satellites in even lower altitudes is necessary to confirm this. It would also be interesting to investigate

the latitudinal variation in the occurrence of LLCs and ADCs for varying K_p and MLT by data from Astrid-2.

The dense 0.1-2 keV ion clouds inside the CPS region observed by Astrid-2 are difficult to understand. None of the three proposed source mechanisms can completely explain them. Simulation of ion flow from the near-Earth plasma sheet does not reproduce the observed energy-latitude dispersion seen in the data. Upward parallel potential drops at the conjugate hemisphere do not usually produce so intense ion fluxes as those in the observed ion clouds: the observed ion fluxes are one order of magnitude higher than the expected ion flux from this scenario. Plasma entry from the magnetosheath does not easily explain the dawn-dusk asymmetry in the data. Thus, the source of the ion clouds still remains unknown. Further study of data (e.g. by the Munin satellite, since it has a nearly identical particle instrument) and simulations are needed to address this question.

Acknowledgments

There are so many people who deserve my thanks either for helping me scientifically or for supporting me in other ways. I will try to name most of them here.

First of all I want to thank Masatoshi Yamauchi and Ingrid Sandahl for being my supervisors during my three years of PhD studies. They have taught me that being a scientist is not supposed to be easy and that nature is, in general, more complex and complicated than any theory. I also want to thank the Swedish Institute of Space Physics and Umeå University for paying my salary, and the Swedish National Space Board for financial support to conferences I have attended as a part of my PhD education.

The scientific discussions with and support and encouragement from Hans Pécseli at the University of Oslo has been of major importance for my PhD-work. He was also one of my supervisors during my Masters studies in Oslo. I also want to thank the Norwegian National Science Foundation for financial support for some of my visits to the University of Oslo.

I have also highly appreciated the scientific discussions I have had with several other scientists: Lars Eliasson, Yusuke Ebihara, Rickard Lundin and Laila Andersson at IRF in Kiruna, Anders Eriksson at IRF in Uppsala, Partik Norqvist at Umeå University, and Jan Trulsen at University of Oslo. Thanks also to Rick McGregor for proof-reading my manuscript. The help from Mikael Hedin and the computer group at IRF on Linux-related problems is greatly appreciated. I also want to thank those of my colleagues who have backed me up during times of frustration.

I do, however, believe that my scientific interest and also my purposive way of working is a result of the support my parents have always given me and also the discussions I had (and still have) with my father on natural science. It is also important that some of my teachers in school, Adelaide Alfsen and Terje Narvesen, helped me to realize my abilities; without it I might not have started my scientific studies.

A special thanks also to my husband, Amund, who has given me great support. I am fortunate to have a husband who encourages me to have a career.

Solveig H. Høymork, February 2001

Bibliography

Akasofu, S.-I. and Chapman, S. (1972). *Solar-Terrestrial Physics*. Clarendon Press.

André, M., editor (1993). *The Freja Scientific Satellite*. Number 214 in IRF Scientific Report. Swedish Institute of Space Physics.

André, M., Norqvist, P., Vaivads, A., Eliasson, L., Norberg, O., Eriksson, A. I., and Holback, B. (1994). Transverse ion energization and wave emissions observed by the FREJA satellite. *Geophys. Res. Lett.*, **21**(17), 1915.

Bell, T. F. and Ngo, H. D. (1990). Electrostatic lower hybrid waves exited by electromagnetic whistler mode waves scattering from planar magnetic-field-aligned plasma density irregularities. *J. Geophys. Res.*, **95**(A1), 149.

Benson, R. F. and Calvert, W. (1979). ISIS 1 observations at the source of auroral kilometric radiation. *Geophys. Res. Lett.*, **6**(6), 479–482.

Bhattacharyya, G. K. and Johnson, R. A. (1977). *Statistical Consepts and Methods*. John Wiley and Sons, Inc.

Blomberg, L. G., Marklund, G. T., P.-A., L., and Bylander, L. (1997). Astrid-2: An advanced auroral microprobe. In *Proc. of COSPAR Colloquium on Scientific Microsatellties*.

Bonell, J. W., Schuck, P. W., Pinçon, J.-L., Seyler, C. E., and Kintner, P. M. (1998). Observation of bound states and counterrotating lower hybrid eigenmodes in the auroral ionosphere. *Phys. Rev. Lett.*, **80**, 5734.

Calvert, W. (1981). The auroral plasma cavity. *Geophys. Res. Lett.*, **8**(8), 919–921.

Chan, Y. T. (1995). *Wavelet Basics*. Kluwer Academic Publishers.

Chen, F. F. (1984). *Introduction to Plasma Physics and Controlled Fusion*, volume 1: Plasma Physics. Plenum Press, 2 edition.

Collin, H. L., Peterson, W. K., Lennartsson, O. W., and Drake, J. F. (1998). The seasonal variation of auroral ion beams. *Geophys. Res. Lett.*

Doe, R. A., Vickrey, J. F., and Mendillo, M. (1995). Electrodynamic model for the formation of auroral ionospheric cavities. *J. Geophys. Res.*, **100**(A6), 9683.

Dovner, P. O., Eriksson, A. I., Boström, R., and Holback, B. (1994). Freja multiprobe observations of electrostatic solitary structures. *Geophys. Res. Lett.*, **21**, 1827.

Dovner, P. O., Eriksson, A. I., Boström, R., Holback, B., Waldemark, J., Eliasson, L., and Boehm, M. (1997). The occurrence of lower hybrid cavities in the upper ionosphere. *Geophys. Res. Lett.*, **24**, 619.

Egeland, A., Sandholt, P. E., and Thrane, E. (1996). Kosmisk Fysikk I, fys 260.

Eliasson, L., Norberg, O., Lundin, R., Olsen, S., Borg, H., André, M., Koskinen, H., Riihelä, P., Boehm, M., and Whalen, B. (1994). The Freja hot plasma experiment - instrument and first results. *Space Science Rev.*, **70**, 563–576.

Ergun, R. E., Klementis, E., Delory, G. T., McFadden, J. P., and Carlsson, C. W. (1995). VLF wave localization in the low-altitude auroral region. *Geophys. Res. Lett.*, **22**(16), 2099–2102.

Eriksson, A. I., Holback, B., Dovner, P. O., Boström, R., Holmgren, G., André, M., Eliasson, L., and Kintner, P. M. (1994). Freja observations of correlated small–scale density depletions and enhanced lower–hybrid waves. *Geophys. Res. Lett.*, **21**, 1843.

Feldstein, Y. I. and Galperin, Y. I. (1985). The auroral luminosity structure in the high-latitude upper atmosphere: Its dynamics and relationship to the large-scale structure of the Earth's magnetosphere. *Rev. Geophys.*, **23**(3), 217.

Freeman, M. O. (1993). Wavelets, Signal Representations with Important Advantages. *Optics and Photonics News.*

Goldston, R. J. and Rutherford, P. H. (1995). *Introduction to Plasma Physics.* Institute of Physics Publishing.

Gulikov, I. A., Zikrach, E. K., Shestakova, L. V., and Starostina, A. S. (1990). The mechanism of formation of the dayside trough during winter in the southern hemisphere. *Geophysical Monograph Series*, **30**(6), 812.

Haerendel, G. (1999). Annual report 1998. MPE report 269, Max-Planck-Institut für extraterrestrische Physik.

Hamrin, M., André, M., Norqvist, P., and Rönnmark, K. (2000). The importance of a dark ionosphere for ion heating and auroral arc formation. *Geophys. Res. Lett.*, **27**(11), 1635.

Holback, B., Åhlén, L., Lundgren, G., Lyngdal, L., Powell, S., and Meyer, A. (1994). The Freja Wave and Plasma Density Experiment. *Space Science Rev.*, **70**(3-4), 577–592.

Holter, Ø. (1994). Wavelet analysis of time series. In *Proceedings of the Cluster Workshop on Data Analysis Tools*, number 371 in ESA SP.

Hultqvist, B., Øieroset, M., and Paschmann, G., editors (1999). *Magnetospheric plasma sources and losses.* ISSI report. Kluwer Academic Publishers.

Johnson, J. R. and Chang, T. (1995). Nonlinear vortex structures with diverging electric fields and their relation to the black aurora. *Geophys. Res. Lett.*, **22**(12), 1481–1484.

Khazanov, G. V., Liemohn, M. W., Krivorutsky, E. N., and Horwitz, J. L. (1997). A model for lower hybrid wave excitation compared with observations by Viking. *Geophys. Res. Lett.*, **24**(19), 2399.

Khazanov, G. V., Gamayunov, K. V., and Liemohn, M. W. (2000). Alfvén waves as a source of lower-hybrid activity in the ring current region. *J. Geophys. Res.*, **105**(A3), 5403.

Klumpar, D. M. (1979). Transversely accelerated ions: An ionospheric source of hot magnetospheric ions. *J. Geophys. Res.*, **84**, 4229.

Knudsen, D. J., Clemmons, J. H., and Wahlund, J.-E. (1998a). Correlation between core ion energization, suprathermal electron bursts, and broad-band ELF plasma waves. *J. Geophys. Res.*, **103**(A3), 4171–4186.

Knudsen, D. J., Dovner, P. O., Eriksson, A. I., and Lynch, K. A. (1998b). Effect of lower hybrid cavities on core plasma observed by Freja. *J. Geophys. Res.*, **103**, 4241.

Knudsen, D. J., Wallis, D. D., and James, H. G. (1999). Tethered two-point measurements of solitary auroral density cavities. *Geophys. Res. Lett.*, **26**(19), 2933.

Kuznetsov, E. A. and Skoric, M. M. (1988). Hierarchy of collapse regimes for upper-hybrid and lower-hybrid waves. *Phys. Rev.*, **38**, 1422.

LaBelle, J., Kintner, P. M., Yau, A. W., and Whalen, B. A. (1986). Large–amplitude wave packets observed in the ionosphere in association with transverse ion acceleration. *J. Geophys. Res.*, **91**(A6), 7113.

Lundin, R. (1997). Observational and theoretical aspects other than merging and diffusion governing plasma transport across the magnetopause. *Space Science Rev.*, **80**, 269–304.

Lundin, R. and Hulqvist, B. (1989). Ionospheric plasma escape by high altitude electric fields: magnetic moment "pumping". *J. Geophys. Res.*, **94**(A6), 6665.

Lundin, R., Haerendel, G., and Grahn, S. (1994a). The FREJA project. *Geophys. Res. Lett.*, **21**, 1823.

Lundin, R., Haerendel, G., and Grahn, S. (1994b). The Freja Science Mission. *Space Science Rev.*, **70**(3-4), 405–419.

Lundin, R., Eliasson, L., Haerendel, G., Boehm, M., and Holback, B. (1994c). Large-scale auroral plasma density cavities observed by Freja. *Geophys. Res. Lett.*, **21**, 1903.

Lynch, K. A., Arnoldy, R. L., Kintner, P. M., and Bonnell, J. (1996). The AMICIST auroral sounding rocket: A comparison of transverse ion acceleration mechanisms. *Geophys. Res. Lett.*, **23**(23), 3293.

Lynch, K. A., Arnoldy, R. L., Kintner, P. M., Schuck, P., Bonnell, J. W., and Coffey, V. (1999). Auroral ion acceleration from lower hybrid solitary structures: A summary of sounding rocket observations. *J. Geophys. Res.*, **104**(A12), 28515–28534.

Lyons, L. R. and Williams, D. J. (1984). *Quantitative aspects of magnetospheric physics.* D. Reidel Publishing Company, second edition. ISBN 90-277-1663-3.

Lysak, R. L. (1991). Feedback instability of the ionospheric resonant cavity. *J. Geophys. Res.*, **96**(A2), 1553.

Mäkelä, J. S., Mälkki, A., Koskinen, H., Boehm, M., Holback, B., and Eliasson, L. (1998). Observations of mesoscale auroral plasma cavity crossings with the Freja satellite. *J. Geophys. Res.*, **103**(A5), 9391.

Marklund, G., Karlsson, T., and Clemmons, J. (1997). On low-altitude particle acceleration and intense electric fields and their relationship to black aurora. *J. Geophys. Res.*, **102**(A8), 17509–17522.

Mayard, P. N. (1980). *Derivation, Meaning, and Use of Geomagnetic Indices*. Number 22 in Geophysical Monograph Series. AGU (American Geophysical Union).

McAdams, K. L., LaBelle, J., Schuck, P. W., and Kintner, P. M. (1998). PHAZE II observations of lower hybrid burst structures occurring on density gradients. *Geophys. Res. Lett.*, **25**(16), 3091.

Muldrew, D. B. (1965). F-layer ionozation troughs deduced from Alouette data. *J. Geophys. Res.*, **70**(11), 2635.

Musher, S. L. and Sturman, B. I. (1975). Collapse of plasma waves near the lower hybrid resonance. *JETP Letters*, **22**, 265.

Newell, P. T. and Meng, C.-I. (1992). Mapping the dayside ionosphere to the magnetosphere according to particle precipitation characteristics. *Geophys. Res. Lett.*, **19**(6), 609.

Newell, P. T. and Meng, C.-I. (1994). Ionospheric projections of magnetospheric regions under low and high solar wind dynamic pressure conditions. *J. Geophys. Res.*, **99**, 273.

Newell, P. T., Meng, C.-I., and Lyons, K. M. (1996). Suppression of discrete aurorae by sunlight. *Nature*, **381**, 766.

Newell, P. T., Meng, C.-I., and Wing, S. (1998). Relation to solar activity of intense aurorae in sunlight and darkness. *Nature*, **393**, 342.

Norqvist, P., Oscarsson, T., André, M., and Blomberg, L. (1998a). Isotropic and perpendicular energization of oxygen ions at energies below 1 eV. *J. Geophys. Res.*, **103**(A3), 4223–4239.

Norqvist, P., André, M., and Tyrland, M. (1998b). A statistical study of ion energization mechanisms in the auroral region. *J. Geophys. Res.*, **103**(A10), 23459–23473.

Østgård, N., Stadsnes, J., Bjordal, J., Vondrak, R. R., Cummer, S. A., Chenette, D. L., Schulz, M., and Pronko, J. G. (2000). Cause of the localized maximum of x-ray emission in the morning sector: A comparison with electron measurements. *J. Geophys. Res.*, **105**(A9), 20869 – 20883.

Pécseli, H. L., Iranpour, K., Holter, Ø., Lybekk, B., Holtet, J., Trulsen, J., Eriksson, A., and Holback, B. (1996). Lower hybrid wave cavities detected by the FREJA satellite. *J. Geophys. Res.*, **101**(A3), 5299.

Persoon, A. M., Gurnett, D. A., Peterson, W. K., Waite, J. H., Burch, J. L., and Green, J. L. (1998). Electron density depletions in the nightside auroral zone. *J. Geophys. Res.*, **93**(A3), 1871.

Retterer, J. M., Chang, T., and Jasperse, J. R. (1986). Ion acceleration by lower hybrid waves in the superauroral region. *J. Geophys. Res.*, **91**, 1609.

Robinson, P. A. (1998). Nonlinear lower hybrid structures in auroral plasmas: comparison of theory with observations. In *COSPAR in Nagoya*. COSPAR (Committee on Space Research).

Rönnmark, K. (1999). Electron acceleration in the auroral current circuit. *Geophys. Res. Lett.*, **26**(7), 983.

Rosenberg, S. and Gekelman, W. (1998). Electric field measurements of directly converted lower hybrid waves at a density striation. *Geophys. Res. Lett.*, **25**(6), 865–868.

Rosenberg, S. and Gekelman, W. (2000). A laboratory investigation of lower hybrid wave interactions with a field-aligned density depletion. *Geophys. Res. Lett.*, **27**(6), 859.

Rycroft, M. J. and Thomas, J. O. (1970). The magnetospheric plasmapause and the electron density trough at the Aluette I orbit. *Planet. Space Sci.*, **18**, 65.

Schuck, P. W., Seyler, C. E., Pincon, J.-L., Bonnell, J. W., and Kintner, P. M. (1998). Theory, simulation, and observation of discrete eigenmodes associated with lower hybrid solitary structures. *J. Geophys. Res.*, **103**(A4), 6935.

Shapiro, V. D., Shevchenko, V. I., Solov'ev, G. I., Kalinin, V. P., Bingham, R., Sagdeev, R. Z., Ashour-Abdalla, M., Dawson, J., and Su, J. J. (1993). Wave collapse at the lower hybrid resonance. *Phys. Fluids*, **B5**, 3148.

Squires, G. L. (1993). *Practical Physics*. Cambridge University Press, 3. edition.

Stasiewicz, K., Gustafsson, G., Lindqvist, P.-A., Clemmons, J., and Zanetti, L. (1997). Cavity resonators and Alfvén resonance cones observed on FREJA. *J. Geophys. Res.*, **102**(A2), 2565–2575.

Thomas, J. O. and Andrews, M. K. (1968). Transpolar exospheric plasma: 1. Plasmasphere termination. *J. Geophys. Res.*, **73**(23), 7407.

Treumann, R. A. and Baumjohann, W. (1997). *Advanced space plasma physics*. Imperial College Press.

Vago, J. L., Kintner, P. M., Chesney, S. W., Arnoldy, R. L., Lynch, K. A., Moore, T. E., and Pollock, C. J. (1992). Transverse ion acceleration by localized lower hybrid waves in the topside auroral ionosphere. *J. Geophys. Res.*, **97**(A11), 16935.

Wahlund, J.-E., Louarn, P., Chust, T., de Feraudy, H., Roux, A., Holback, B., Dovner, P.-O., and Holmgren, G. (1994). On ion acoustic turbulence and the nonlinear evolution of kinetic Alfvén waves in aurora. *Geophys. Res. Lett.*, **21**(17), 1831–1834.

Winningham, J. D., Yasuhara, F., Akasofu, S.-I., and Heikkila, W. J. (1975). The latitudinal morphology of 10-eV to 10-keV electron fluxes during magnetically quiet and disturbed times in the 2100-0300 MLT sector. *J. Geophys. Res.*, **80**, 3148.

Winningham, J. D., Burch, J. L., and Frahm, R. A. (1984). Bands of ions and angular V's: A conjugate manifestation of ionospheric ion acceleration. *J. Geophys. Res.*, **89**, 1749.

Zakharov, V. E. (1972). Collapse of Langmuir waves. *J. Exp. Theor. Phys.*, **35**, 908.

Appendix A
Lower hybrid waves and magnetosonic waves

The main part of this thesis concentrates on lower hybrid cavities and this phenomenon is therefore further discussed here. A large number of lower hybrid cavities (LHCs) (also called lower hybrid solitary structures) have been observed by the Freja satellite (see section 1.8.1 and Paper I, II and III). LHCs are accompanied by lower hybrid waves and we recall that these waves are electrostatic ($E/B \rightarrow \infty$). However, wave data inside areas containing LHCs sometimes show electromagnetic wave (finite E/B) components at frequencies below that of the observed lower hybrid wave. This electromagnetic wave is often clearly separated from the lower hybrid wave in frequency, and it also has a lower amplitude. This wave can most probably be interpreted as the magnetosonic wave (see Section 1.6.3).

Two wave components can also be seen when we investigate individual cavities. Here the upper frequency is interpreted as a propagating mode, and the lower frequency as a trapped mode. In such cases the lowest frequency will often be electrostatic.

The following sections will provide observations and discussion of these wave phenomena both on a large scale (Section A.1) and on the scale of individual cavities (Section A.2).

A.1 Large-scale wave structures

As mentioned in section 1.6, the frequency is one of the main characteristics in classification of waves. The Fourier transform (Appendix B) of a time-series of data provides its frequency spectrum, and this enables separation of different types of waves.

Figure A.1 shows FFT (fast Fourier transform) of the magnetic and electric fields and also the variation in total plasma density during Freja orbit 6663 (February 22, 1994) and 1547 (January 31, 1993). Note that the magnetic and electric fields were sampled in bursts mode with burst length of $\sim$ 16 ms (frequency range 1 Hz – 16 kHz) and $\sim$ 2 s intervals between the bursts. Magnetic and electric fields were not measured simultaneously and can thus only be compared on a large scale ($>$ 10 s). The absolute plasma density is also plotted. The regions where LHCs are observed are marked in the plots and here we are interested in the waves inside these regions. We recall that since individual cavities are observed during a time period of only $\sim$ 2 ms they are not discernable in this plot.

The electric and magnetic field spectrograms in Figure A.1 show the electrostatic lower hybrid wave at a frequency of about 4 kHz. The spectrograms also show an additional electromagnetic wave at lower frequency. This electromagnetic wave is most easily explained as a magnetosonic wave.

The lower hybrid frequency in Figure A.1 seems to grow as the plasma density increases. This indicates that these waves are probably exited locally and have not traveled from a

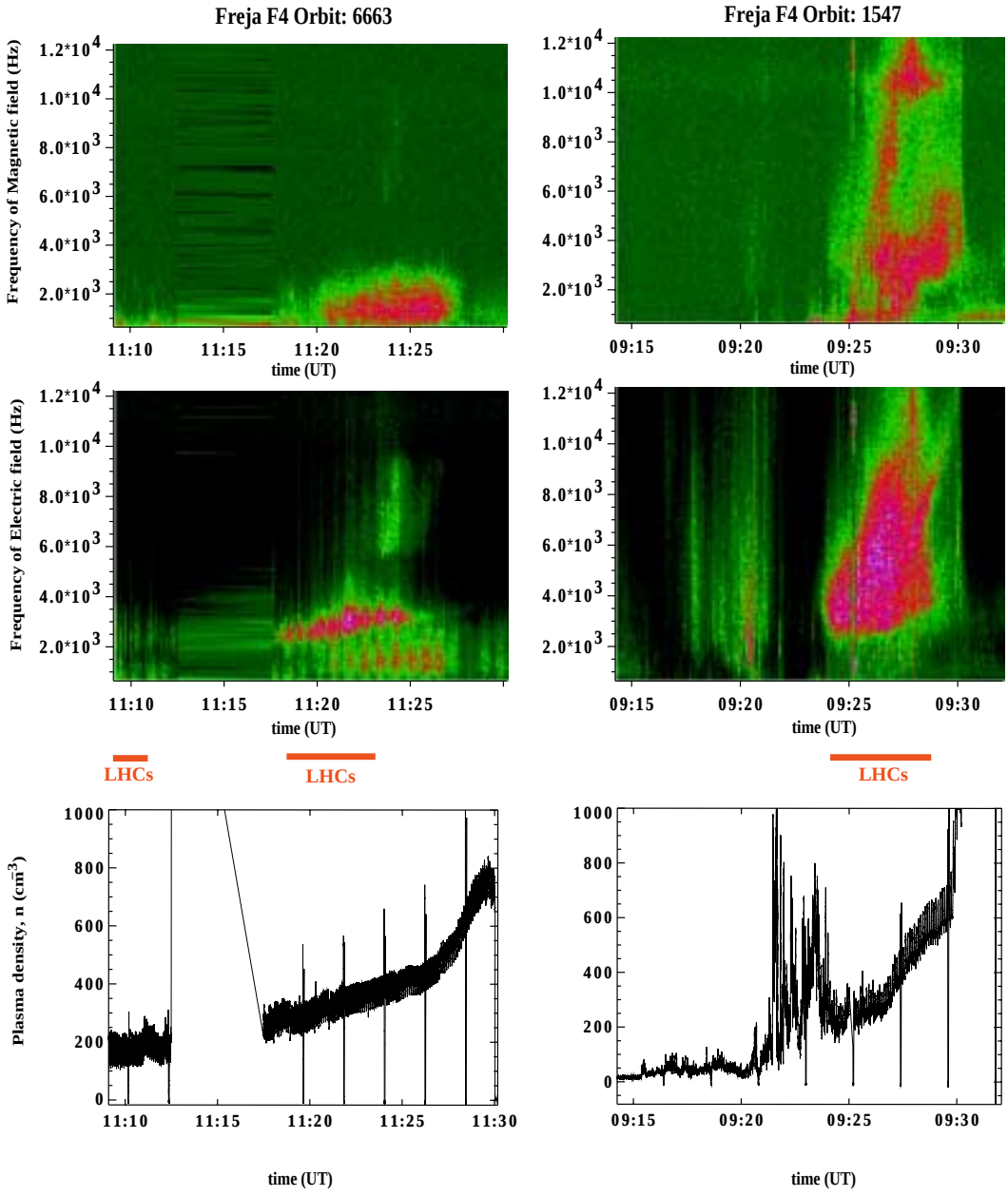

Figure A.1: FFT of the magnetic (upper panels) and electric (middle panels) fields, and absolute plasma density (lower panels) of orbit 6663 and orbit 1547. Regions where LHCs are observed are marked with red lines in the plots. Note that the electric and magnetic fields are not sampled simultaneously and can thus not be compared on small timescales for these orbits. (The time-period between 11:25.5 UT and 11:17.5 UT in orbit 6663 contains no medium frequency electric or magnetic field or density data.)

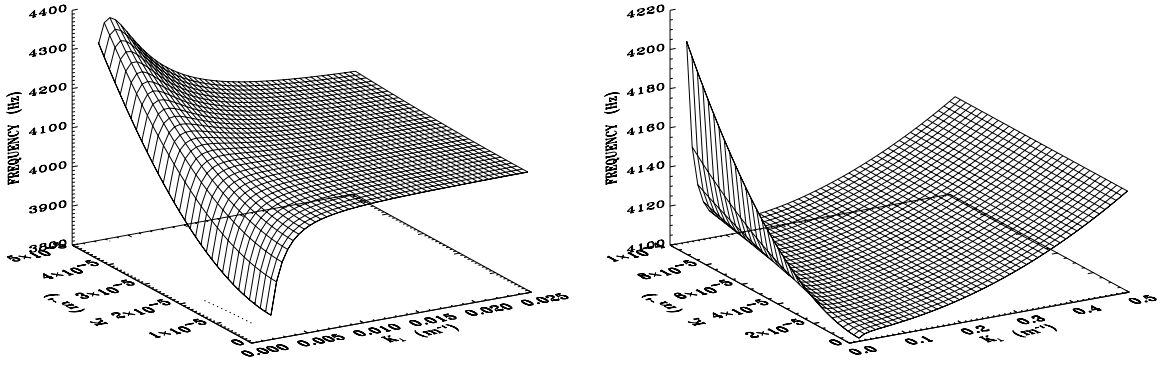

Figure A.2: Dispersion relation for lower hybrid waves obtained by a numerical solution of the full plasma kinetic dispersion relation with B= 40 nT, n_e = 500 cm^{-3}, n_{O^+}/n_{H^+} = 0.3 and $T_e = T_i$ = 0.2 eV. Both the low wave number (left) and high wave number (right) ranges are shown. (Note that more than one ion species in the calculation results in the bend-over for small $k_\perp$ also for larger $k_\parallel$.) (Plot by Jan Trulsen, University of Oslo.)

common source. The only other possible explanation for this density dependence on the frequency is that the frequency is significantly changed due to Doppler-shift as a result of local change in wavelength. It can, however, be shown (see Appendix C) that this Doppler-shift correction is small for frequencies in the lower hybrid range when measured by the probes on board Freja.

We know from theory (see section 1.6.3) that the magnetosonic wave has a phase velocity close to the Alfvén velocity, in the low frequency limit. The Alfvén velocity, V_A, in the auroral/sub-auroral zone at Freja's altitude can be calculated, with $\rho = \sum_{allspecies,i} n_{0i} m_i$, where $n_0 = 500$ cm^{-3}, a mixing ratio of O^+:H^+:He^+ =90:10:1, and $B_0 \sim 0.3 \cdot 10^{-4}$ T:

$$V_A = B_0/(\mu_0 \rho)^{1/2} \sim 10 \text{ Mm/s} \tag{A.1}$$

where μ_0 is the permeability of free space ($4\pi \times 10^{-7}$ H/m). For purely transversal waves (as magnetosonic waves) E/B equals the phase velocity and in this case the Alfvén speed. For purely electrostatic waves on the other hand, E/B becomes infinity, and hence $E/B \gg V_A$.

We note that magnetosonic waves and lower hybrid waves are not to be seen as two completely unrelated waveforms. As outlined in section 1.6 they are the lower and upper, respectively, wave number (frequency) solutions to the same dispersion relation (the lower hybrid wave dispersion relation) as outlined in section 1.6.1. The left panel in Figure A.2 shows the small wave number (long wavelength) part of this dispersion relation for parameters relevant at Freja's height, where the cold plasma resonance cone (the third term in Eq. 1.32) dominates. This gives the bend-over (frequency decrease) for small $k_\perp$ observed in Figure A.2. At these wave numbers, the wave changes from electrostatic to electromagnetic, i.e. into the magnetosonic wave. The higher wavelength part ($k_\perp > 0.01$ m^{-1}), which is the electrostatic lower hybrid wave, is also plotted in Figure A.2 (right panel).

To enable comparison and identification of the two different waves in Figure A.1 we also provide bandpass-filtered electric and magnetic fields in two different frequency bands. The first frequency band is chosen between 1 kHz and 2 kHz and the second between 2.5 kHz and 4

kHz. These bands are chosen to roughly separate the electrostatic (upper) and electromagnetic (lower) frequency regions seen in Figure A.1. Figure A.3 and Figure A.4 show bandpass-filtered electric and magnetic fields for orbit 1547 and 6663. In addition, the bottom panel of each figure also gives the E/B-ratio for the two frequency bands. In most cases only one component of the electric field and one component of the magnetic field are available (as for the orbits discussed here), but by averaging this ratio over periods longer than a satellite spin (approximately 6 sec.) we can obtain a fairly good estimate of the E/B-ratio. The E/B-ratio is in the order of the Alfvén velocity ($V_A \sim 10$ Mm/s) for the lower frequency band and it is ten times greater than the Alfvén velocity for the higher frequency band.

This indicates that the lower hybrid waves in the investigated orbits are most probably accompanied by magnetosonic waves. One interpretation of the observed wave data could be that the magnetosonic wave is simply the low frequency continuation of the lower hybrid wave, as outlined in Figure A.2. One problem associated with this explanation is that it does not account for the clear separation between the lower hybrid and magnetosonic waves seen for orbit 6663 in Figure A.1. We see no *a priori* reason for a separation between the two modes if the magnetosonic wave is a pure continuation of the lower hybrid wave for lower frequencies.

One might, however, also argue that the lower hybrid waves could have been generated by the magnetosonic waves. Theoretical investigations by Khazanov *et al.* [1997] and by Bell and Ngo [1990] have shown that lower hybrid waves can be generated by magnetosonic waves. The fact that the observed lower hybrid waves are generated locally, as argued above, opens the possibility for such a generation mechanism by the accompanying magnetosonic waves. The magnetosonic waves are, however, seen almost solely together with lower hybrid waves. This indicates that either the generation mechanism for lower hybrid waves is so efficient that a magnetosonic wave in the given environment (density, magnetic field strength, ion composition, etc.) always generates lower hybrid waves, or there must be another connection between the two waves.

A.2 Trapped and propagating modes

The previous discussion was concerned with large scale ($\sim$ minutes along Freja's orbit, i.e. $\sim$ 500 m) electric and magnetic field variations. The remaining question then is how these large scale waves are associated with individual LHCs ($\sim$ milliseconds along Freja's orbit, i.e. $\sim$ 50 m). It is, unfortunately, impossible to compare all the magnetic fields and electric fields (in the frequency range of lower hybrid waves), as well as relative plasma density, on this scale since Freja did not measure all these quantities simultaneously. We do, however, have simultaneous measurements of magnetic field (dB) and relative plasma density (dn/n), or simultaneous measurements of magnetic (dB) and electric field (dE) inside individual lower hybrid cavities, as shown in Figure A.5. Other plots of simultaneous measurements of electric field and relative plasma density are shown e.g. in Paper I and II of this thesis.

The electric and magnetic field data in Figure A.5 are displayed by the use of wavelet transform. The wavelet transform (Appendix B) is similar to the fast Fourier transform but it is optimized for the best frequency and time resolution and can be used for investigation of continuous time series of data.

The simultaneous measurements of dB and dn/n in Figure A.5 (left) show no wave signature in the magnetic field inside the cavity. The amplitude of the magnetic field is the same inside

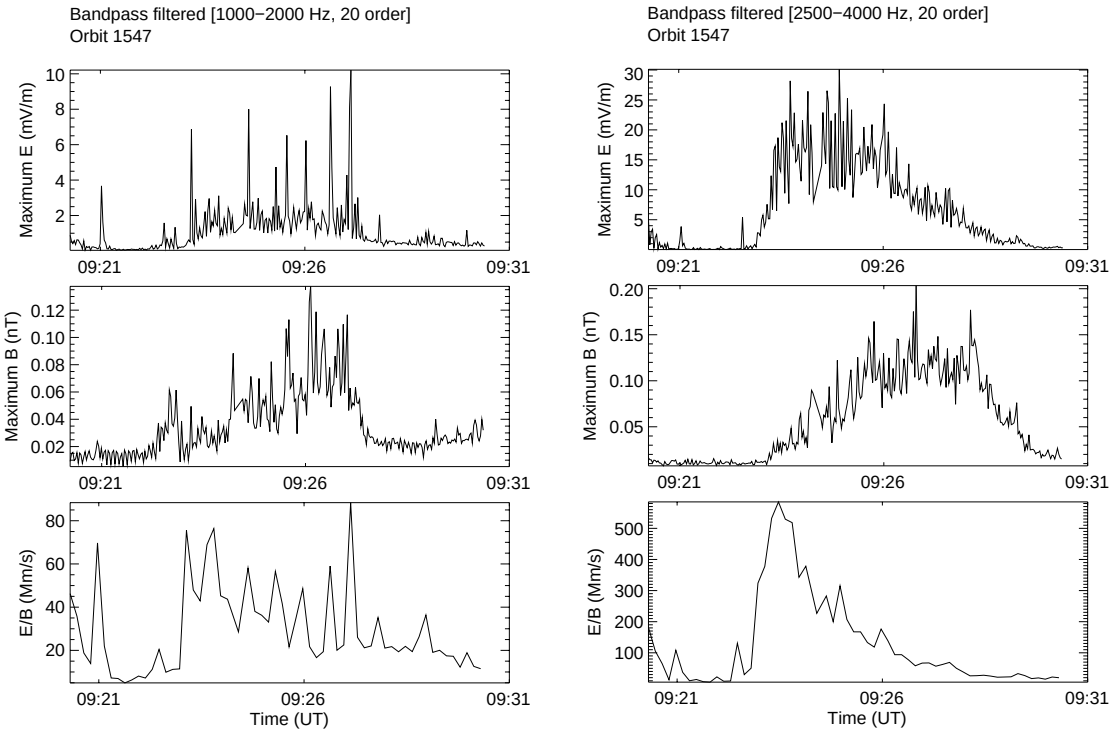

Figure A.3: Bandpass filtered electric and magnetic fields from orbit 1547. The left hand panel shows bandpass filtering between 1000 Hz and 2000 Hz and the right hand panel shows bandpass filtering between 2500 Hz and 4000 Hz. The upper plots are electric fields, the middle plots are magnetic fields and the lower plots are the E/B-ratio.

and outside the cavity as is the wavelet transform. From previous observations we have seen that these cavities were correlated with wave signatures in the electric field (see e.g. Paper I). For the case observed in Figure A.5 (left), we therefore expect that an electrostatic wave exist, although we did not explicitly measure it in this case.

To further investigate the nature of these waves we also compare simultaneous measurements of magnetic field fluctuations, dB, and electric field fluctuations, dE (right panels in Figure A.5). The LHC is in this case identified by the electric field signature. This signature is not accompanied by a similar magnetic field signature. The magnetic field has a much lower amplitude than the electric field and the wavelet transform of the magnetic field shows no enhancement of the wave amplitude around the frequency observed in the electric field. The magnetic field amplitude seems instead to be lower inside the LHC than outside, at least in the lower hybrid frequency range. This is a common feature seen in many cases and this also strongly indicates that these waves are electrostatic.

The wavelet transform of the electric field in Figure A.5 (right) shows two frequency bands, one around 4 kHz and the other around 2 kHz. Similar signatures have been reported by e.g. Pécseli *et al.* [1996] and Paper I of this thesis. These are interpreted as a propagating mode (the highest frequency) and a trapped mode (the lower frequency). Both the propagating mode and the trapped mode in Figure A.5 seem to be electrostatic although the amplitude of the magnetic field is slightly higher for the trapped mode.

Figure A.6 shows the bandpass-filtered E/B-ratio for the simultaneous electric and mag-

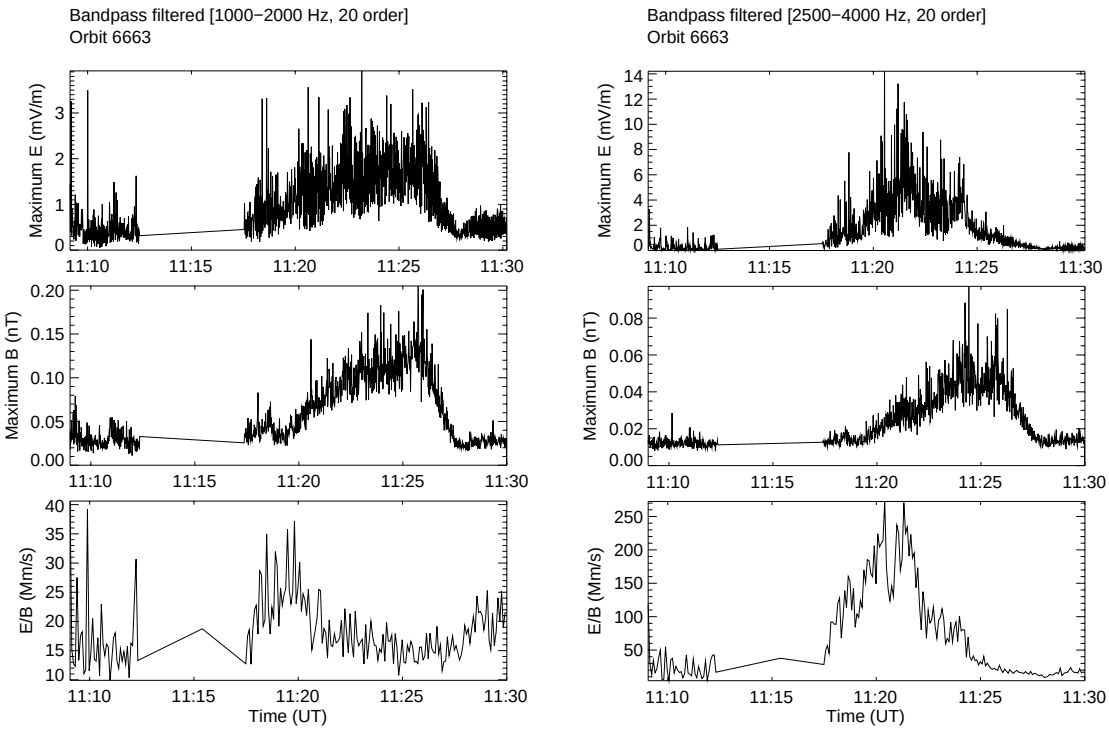

Figure A.4: Bandpass filtered electric and magnetic fields, similar to Figure A.3, from orbit 6663.

netic fields in Figure A.5 (right). This figure indicates that both the high frequency and the low frequency modes are electrostatic. The lowest frequency mode has a lower E/B-ratio (100-900 Mm/s) than the highest frequency mode (500-4000 Mm/s).

A.3 Discussion

Electromagnetic waves, which are identified as magnetosonic waves, are observed inside areas of lower hybrid waves and density cavities. They might play a role in the generation of the lower hybrid waves. The fact that the frequency of the lower hybrid waves varies with the local plasma density indicates that these waves are generated locally since the Doppler shift correction is small (Appendix C). The magnetosonic waves are, however, only observed together with the lower hybrid waves, which indicates either that the generation mechanism is so efficient that lower hybrid waves are always generated, or that they are connected in some other way. The magnetosonic waves may also simply be the low frequency continuation of the observed lower hybrid waves. One problem here is the general lack of gradual transition seen in spectrograms between the two types of wave. The two waves are usually separated by an "empty" frequency band.

Two different wave modes are also observed on the scale of individual cavities: one is a propagating mode (at highest frequency) and the other is a trapped mode (at lowest frequency). Both of the two wave modes are electrostatic, although the lowest frequency mode seems to have the largest magnetic field component. The lowest frequency here is therefore not the magnetosonic wave.

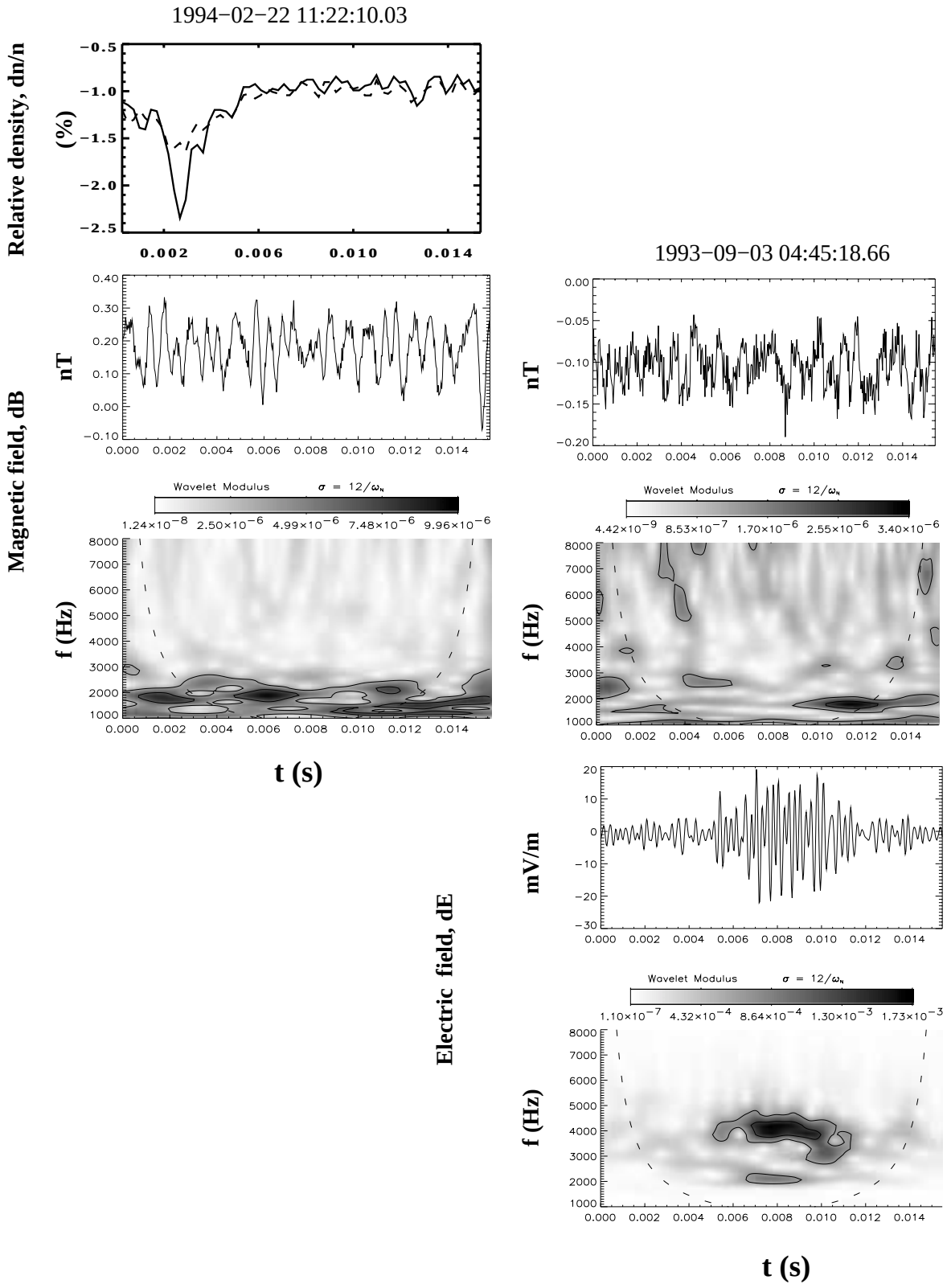

Figure A.5: Simultaneous measurements of relative plasma density (dn/n) and magnetic field (dB) on the left, and simultaneous measurements of magnetic (dB) and electric field (dE) on the right, of individual lower hybrid cavities. Electric and magnetic fields are presented as time-series (line plot) and by wavelet transform (spectrogram).

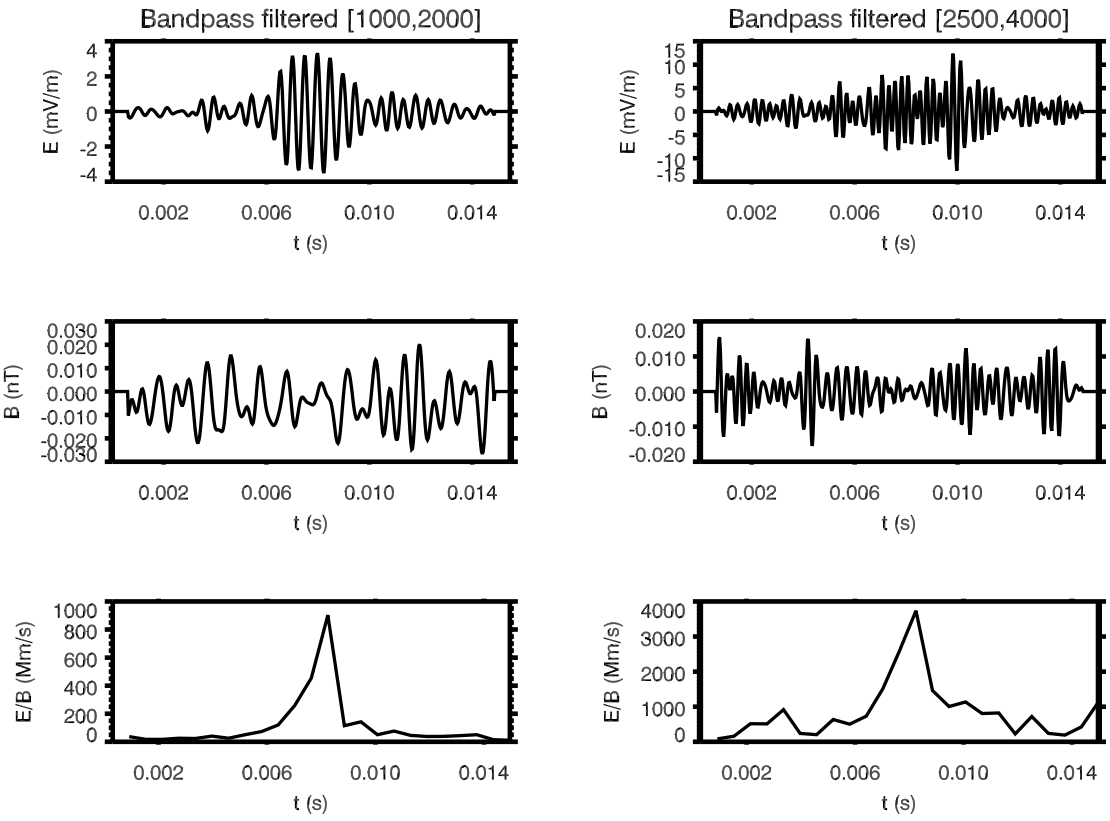

Figure A.6: Bandpass filtration of the simultaneous electric and magnetic fields shown in the right panels of Figure A.5.

The magnetosonic waves may therefore play a role in the generation of lower hybrid waves, but they exist only outside the cavities, and do not seem to be significant for cavity formation.

Appendix B
Frequency analysis of timeseries

This chapter is written primary after reading Chan [1995], Freeman [1993] and Holter [1994].

B.1 Fourier transform

In general a transform of a timeseries, $s(t)$ is a mathematical operation that results in a different representation of $s(t)$ in terms of the building blocks, or basis functions, of the transformed domain. The Fourier transform of a timeseries gives the frequency spectrum of the signal, and in this domain the building blocks are sinusoids. The signal is uniquely represented in the Fourier domain by a sum of sinusoids with different amplitudes, frequencies (ω), and phases. The forward Fourier transform is defined by

$$S(\omega) = \int_{-\infty}^{\infty} s(t) e^{-j\omega t} dt, \tag{B.1}$$

and it decomposes the timeseries, $s(t)$, into a complex sinusoidal function, $S(\omega)$. This has a frequency ω, amplitude $|S(\omega)|$, and phase $S(\omega)/|S(\omega)|$. The inverse Fourier transform is correspondingly defined by

$$s(t) = \frac{1}{2\pi} \int_{-\infty}^{\infty} S(\omega) e^{j\omega t} d\omega, \tag{B.2}$$

and it synthesizes the timeseries, $s(t)$, from the basis functions $e^{j\omega t}$ of complex amplitude $S(\omega)$.

The Fourier frequency spectrum $S(\omega)$ is independent of time and it is therefore not very useful to represent non-stationary or transient signals. It does not contain any information on the changes in the frequency spectrum with time. Real data often show a change of $S(\omega)$ in time and this is the motivation for the windowed Fourier transform.

B.2 Windowed Fourier transform

A natural way to compute a local spectrum is to apply the Fourier transform to one local piece of the signal at a time. This is the idea behind the windowed Fourier transform (WFT)

$$F(\omega, \tau) = \int_{-\infty}^{\infty} s(t) g^*(t - \tau) e^{-j\omega t} dt, \tag{B.3}$$

where g(t) is some window function that is non-vanishing only in a region around $t = \tau$, and * denotes the complex conjugate. The WFT thus gives the frequency spectra of the signal at different positions by moving the window to these positions. The simplest form of this transform uses a rectangular window.

The choice of window function may severely affect the frequency spectra that is obtained. The width of the window function is especially important. A rectangular window with infinite width will result in the original Fourier transform, $F(\omega)$. The window functions, $g(t)$, used in WFT are independent of frequency. One therefore has to choose between high resolution in time (narrow window) or high resolution in frequency (wide window). A wide window will give a good frequency resolution since it enables detection of lower frequency waves (i.e. window size $\sim$ wave period), but this also gives a poor time resolution. A narrow window will, on the other hand, result in low frequency resolution but high time resolution. It is thus a limit to how well the frequency content of a signal at a given time, $\omega(t)$, can be known simultaneously with knowing the time of observation, t. This limit is given by the Uncertainty Principle. This principle states that for any transform pair $s(t)$ and $S(\omega)$,

$$\Delta_t \Delta_\omega \geq \frac{1}{2}, \tag{B.4}$$

where

$$\Delta_t^2 = \frac{\int t^2 |s(t)|^2 dt}{\int |s(t)|^2 dt} \tag{B.5}$$

and

$$\Delta_\omega^2 = \frac{\int \omega^2 |S(\omega)|^2 d\omega}{\int |S(\omega)|^2 d\omega} \tag{B.6}$$

are measures of the variations or spread of $s(t)$ and $S(\omega)$. This uncertainty arise because the signal must be observed for at least a period of time that is equal to the period corresponding to the chosen frequency to enable identification of that frequency in the signal.

B.3 Principles of the wavelet transform

The wavelet transform can give an optimum time and frequency resolution of a time-varying signal under the uncertainty condition (Eq. B.4). This is done by scaling the basis functions (wavelets) for different frequencies. The time shift of the window is given by τ as in WFT, but in addition its width is adjusted to the frequency being analyzed by a scaling parameter a. In this way the uncertainty in the signal and frequency are adjusted according to what type of information is being extracted. In practice this means that a larger window will be used for low frequencies than for high frequencies.

The continuous wavelet transform of $s(t)$ is defined as

$$W(a,\tau) = \frac{1}{\sqrt{a}} \int_{-\infty}^{\infty} s(t) \psi^* \left(\frac{t-\tau}{a} \right) dt, \tag{B.7}$$

where $\psi(t)$ is the basis (or mother) wavelet, $\psi((t-\tau)/a)/\sqrt{a}$ the basis functions (sometimes called baby wavelets), and * denotes the complex conjugate. The basic wavelet can be real or complex, corresponding to a real or complex wavelet transform. The complex wavelet transform coefficients can be expressed in terms of the modulus $|W(a,\tau)|$ and the phase α:

$$W(a,\tau) = |W(a,\tau)| e^{i\alpha}. \tag{B.8}$$

There are four different types of wavelet transforms: the continuous wavelet transform (t, a, and τ are all continuous), the discrete parameter wavelet transform (a and τ are discrete),

the discrete time wavelet transform (t is discrete), and the discrete wavelet transform ($\psi(k)$ is discrete). The rest of this appendix will discuss the continuous wavelet transform (as given in Eq. B.7) only.

The signal $s(t)$ to be transformed by the wavelet transform is assumed to be square integrable

$$\int_{-\infty}^{\infty} s^2(t)dt < \infty, \tag{B.9}$$

and hence it should not be a DC signal nor a pure sinusoid.

For any transform it is important that the transform have an inverse. The Resolution of identity states that for a transformation to be invertible the signal energy in the original domain must be equal to, within a constant, the signal energy in the transformed domain. If the continuous wavelet transform is invertible, then

$$s(t) = \frac{1}{C_\psi} \int_{-\infty}^{\infty} \int_{a>0}^{\infty} W(a,\tau) \frac{1}{\sqrt{a}} \psi\left(\frac{1-\tau}{a}\right) \frac{1}{a^2} \, da \, dt, \tag{B.10}$$

where C_ψ is a constant that depends only on $\psi(t)$, and a is positive. The constant, C_ψ, has a value

$$C_\psi = \int_0^{\infty} \frac{|\psi(\omega)|^2}{\omega} \, d\omega < \infty. \tag{B.11}$$

This in turn imposes an admissibility condition (zero average) on $\psi(t)$, since for $C_\psi < \infty$, $\psi(t)$ must be such that

$$|\psi(\omega)| < \infty \text{ , for any } \omega, \tag{B.12}$$

and $\psi(0) = 0$, implying that

$$\int_{-\infty}^{\infty} \psi(t) \, dt = 0 \tag{B.13}$$

This means that $\psi(t)$ must be oscillatory in nature.

One type of wavelet is the Morlet (Modulated Gaussian) mother wavelet (see Figure B.1), given by

$$\psi(t) = \frac{1}{\sqrt{2\pi}\sigma} e^{i\omega_0 t} e^{-\frac{t^2}{2\sigma^2}}, \tag{B.14}$$

where ω_0 is the basic wavelet frequency and σ determines the width of the Gaussian envelope. The Morlet wavelet, which is constituted by a few oscillations within a Gaussian envelope, does not fulfill the admissibility condition, i.e. we have

$$\int_{-\infty}^{\infty} \psi(t) \, dt = e^{-\sigma^2\omega_0^2/2} > 0. \tag{B.15}$$

For $\sigma\omega_0 \gg 1$, however, the integral becomes very small. Thus, with a sufficient number of wave-periods inside the Gaussian envelope, $\sigma\omega_0 > 5$ for instance, the admissibility condition is almost fulfilled.

The results from a wavelet transform are usually presented in diagrams with time versus frequency with color scale of modulus or phase. Figure A.5 shows examples of wavelet-transforms with modulus/amplitude in a black-white scale. These are called spectrograms.

In this thesis the wavelet transform is used to measure the frequency spectrum of the electric field inside a lower hybrid cavity. It was important to know the position (time of observation)

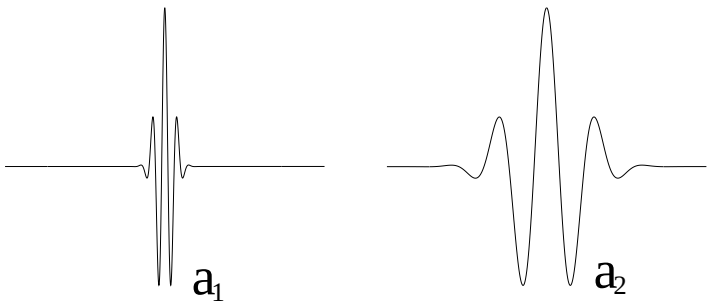

Figure B.1: Morlet (Modulated Gaussian) wavelet with different scalings a, $a_1 < a_2$. In wavelet analysis, short windows (small a) are used for high frequencies while long windows (large a) are used for low frequencies.

of the detected frequencies, so a simple Fourier transform would not give detailed enough information in this study.

An example of the difference between Fourier transform and wavelet transform can be visualized by supposing they were both carried out for the sound of a concert. In the Fourier transform we could see which tones where played during the concert, but not when they where played. The wavelet transform, on the other hand, would give a detailed scheme of all of the tones and when they were played. The human ear is in a sense functioning like a wavelet transform for acoustic waves which makes it possible for us to enjoy music.

Appendix C
The relationship between observed and true electric field

The Freja satellite measured electric wave fields using two Langmuir probes which had a separation distance of 21 or 11 meters (Δ), depending on which probes were used (see Figure C.1). A more detailed description of the wave experiment on board Freja is given by Holback *et al.* [1994].

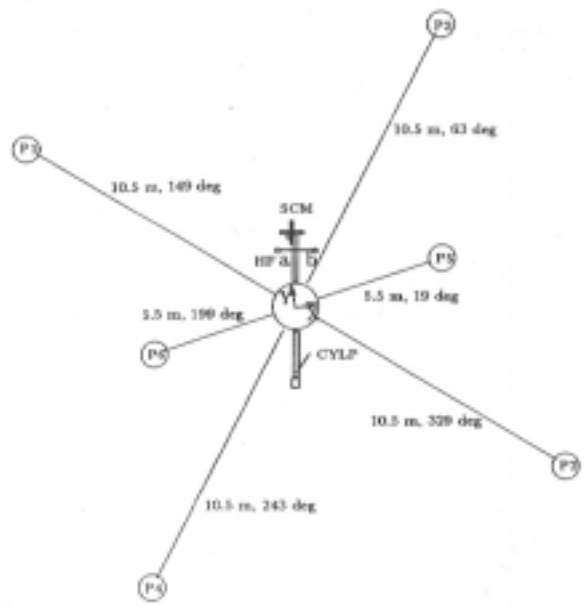

Figure C.1: The boom configuration on Freja.

In a finite data-point measurement, the potential of electrostatic waves is expressed in the form:

$$\Phi = a_j \sin(\omega_j t - \mathbf{k}_j \cdot \mathbf{r}) + b_j \cos(\omega_j t - \mathbf{k}_j \cdot \mathbf{r}), \tag{C.1}$$

where $\mathbf{r}$ is the vector from a fixed point in space to the point where the potential is measured, t is time, and k_j and ω_j are respectively the wave vector and the frequency of the wave. Then the E-field measured by the potential difference between two points in space separated with Δ would be:

$$\mathbf{E}_{mes} = \frac{(\Phi_1 - \Phi_2)}{\Delta} \tag{C.2}$$

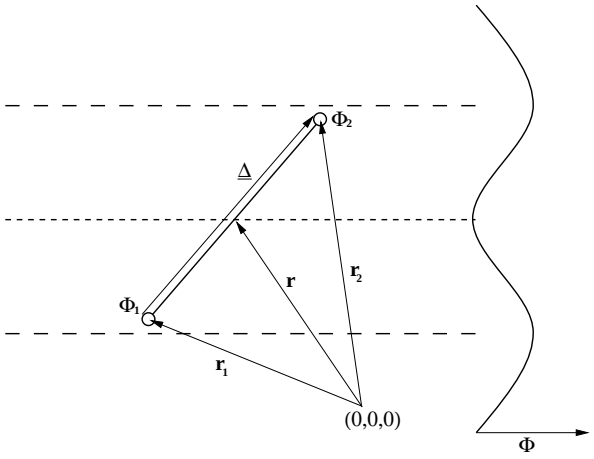

Figure C.2: The geometry for measurements of electric field as the potential difference between two probes.

$$= \frac{a_j \sin(\omega_j t - \mathbf{k}_j \cdot \mathbf{r}_1) + b_j \cos(\omega_j t - \mathbf{k}j \cdot \mathbf{r}_1) + a_j \sin(\omega_j t - \mathbf{k}_j \cdot \mathbf{r}_2) + b_j \cos(\omega_j t - \mathbf{k}_j \cdot \mathbf{r}_2)}{\Delta}, \tag{C.3}$$

with Φ_1 and Φ_2 being the potential at $\mathbf{r}_1$ and $\mathbf{r}_2$ respectively. The geometry of this is sketched in Figure C.2. The true E-field at the satellite position is given by:

$$\mathbf{E}_{true} = -\nabla\Phi \tag{C.4}$$

$$= a_j \mathbf{k}_j \cos(\omega_j t - \mathbf{k}_j \cdot \mathbf{r}) - b_j \mathbf{k}_j \sin(\omega_j t - \mathbf{k}_j \cdot \mathbf{r}), \tag{C.5}$$

where $\mathbf{r}_1 = \mathbf{r} - \frac{1}{2}\underline{\Delta}$ and $\mathbf{r}_2 = \mathbf{r} + \frac{1}{2}\underline{\Delta}$ ($\underline{\Delta}$ is the distance between $\mathbf{r_1}$ and $\mathbf{r_2}$), and hence:

$$\mathbf{E}_{mes} = \frac{[a_j \cos(\omega_j t - \mathbf{k}_j \cdot \mathbf{r}) - b_j \sin(\omega_j t - \mathbf{k}_j \cdot \mathbf{r})] 2 \sin(\frac{1}{2}\mathbf{k}_j \cdot \underline{\Delta})}{\Delta} \tag{C.6}$$

$$= \mathbf{E}_{true} \cdot \frac{\sin(\frac{1}{2}\mathbf{k}_j \cdot \underline{\Delta})}{\frac{1}{2}\mathbf{k}_j \cdot \underline{\Delta}}. \tag{C.7}$$

The last term is the sinc-function, and it is plotted in Figure C.3.

We see from Figure C.3 that E_{mes} will be lower than E_{true} when $\frac{1}{2}\mathbf{k}_j \cdot \underline{\Delta} \neq 0$. To be able to assume that the measured electric field is close to the true electric field ($\mathbf{E}_{mes} \approx \mathbf{E}_{true}$), we need $1/2 < \sin(\frac{1}{2}\mathbf{k}_j \cdot \underline{\Delta})/\frac{1}{2}\mathbf{k}_j \cdot \underline{\Delta} < 1$, which implies, as seen in Figure C.3, that $\frac{1}{2}\mathbf{k} \cdot \underline{\Delta} < \frac{1}{2}\pi$. The angle between $\mathbf{k}$ and $\underline{\Delta}$ will vary with the satellite spin.

Since the satellite was moving with velocity V_0, we also have to consider the Doppler shift correction to the observed frequency. This correction is given by

$$\omega_{obs} = \omega_{true} + \mathbf{k} \cdot \mathbf{V}_0, \tag{C.8}$$

where ω_{obs} is the observed frequency while ω_{true} is the actual frequency of the wave. From Eq. C.8 it is possible that the observed frequency mainly reflects the Doppler shift and not the original wave if $\omega_{true} \lesssim \mathbf{k} \cdot \mathbf{V}_0$. We will in the following consider the Doppler shift correction to the lower hybrid waves observed by Freja.

If the main part of the measured frequency comes from Doppler shift, then

$$\omega_{obs} \approx \mathbf{k} \cdot \mathbf{V}_0 = k_v V_0,$$

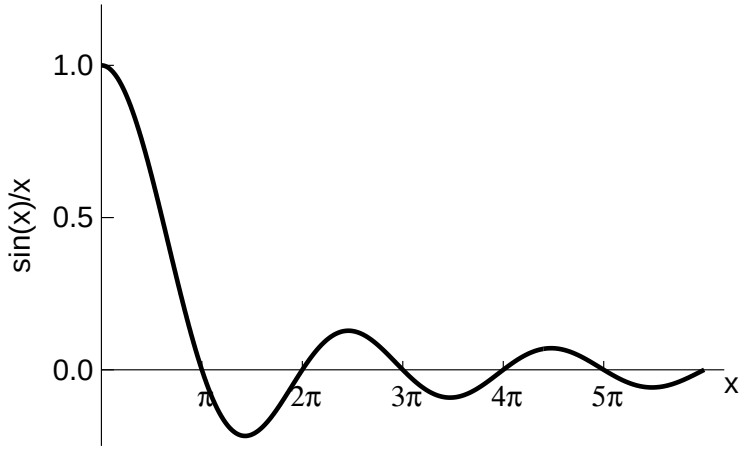

Figure C.3: Plot of the sinc-function, sin(x)/x.

where k_v is the component of $\mathbf{k}$ parallel to $\mathbf{V}_0$ and $\omega_{obs} = 2\pi f_{obs}$. For the actual lower hybrid waves measured by Freja, we have $V_0 \approx 7$ km/s and $f_{obs} \approx 4$ kHz, which give a value of

$$k_v \sim \frac{4}{3.5}\pi \text{ m}^{-1}.$$

If $\underline{\Delta}$ is parallel to $\mathbf{V}_0$ then

$$\mathbf{k} \cdot \underline{\Delta} = k_v \Delta \sim 2\pi \cdot 10$$

This result, however, implies that $\mathbf{E}_{mes} \ll \mathbf{E}_{true}$, according to Figure C.3, and that true electric fields up to 1 V/m exist. Such large electric fields would give wave energy densities comparable to the thermal energy density of the plasma. This is very unlikely. Therefore the Doppler shift correction must, under these conditions, be negligible compared to the true frequency.

From these arguments we can take the measured E-field and frequency to be close to the true E-field and frequency. The measured electric field is always in the range of the actual electric field and never greater than it (it can be a little smaller).

Appendix D
Sensitivity of the Freja TICS instrument

Lower hybrid cavities (LHCs) have been discussed in section 1.8.1 and Appendix A. This appendix discusses the fact that Freja did not observe energized ions inside LHCs.

LHCs have been observed by sounding rockets: Marie [LaBelle *et al.*, 1986], Topaz II and III [Vago *et al.*, 1992], Amicist [Lynch *et al.*, 1996], Phaze II [McAdams *et al.*, 1998], and Oedipus-C [Knudsen *et al.*, 1999], and also by the Freja satellite [e.g. Dovner *et al.*, 1994; Pécseli *et al.*, 1996, and Papers I, II and III of this thesis]. There is, however, a definite difference between rocket and satellite observations of LHCs: in rocket experiments ion energization is seen inside the cavities, but no similar signature is observed by the ion instrument (TICS) on the Freja satellite [André *et al.*, 1994, and Paper III of this thesis]. It has been proposed that this might be due to too low a geometric factor or signal-to-noise (S/N) ratio on the TICS (Three-Dimensional Ion Composition Spectrometer) instrument.

Here we present simulations of the ability of the TICS instrument to resolve ion energization inside cavities in order to distinguish whether this discrepancy is due to instrumental limitations or real physical effects. Plasma properties such as temperature, ion distribution, and density will be varied in the simulation, and we compare the result with the LHC ion energization events observed by rocket experiments [Lynch *et al.*, 1999]. We note that a study of LHC ion energization by the cold plasma analyzer on Freja did show ion flux bursts inside areas containing LHCs, but it did not find any clear correlation between LHCs and these ion bursts [Knudsen *et al.*, 1998b]. However, LHC ion energization was not observed during the Scifer mission, [as mentioned by Lynch *et al.*, 1999] nor by the Alaska UCB'93 rocket [as reported by Delory *et al.* on the 2nd EGS Alfvén Conference]. The Scifer rocket was launched into the dayside auroral zone while the Alaska UCB'93 rocket and the above mentioned rockets were all measuring in the pre-midnight auroral zone.

This Appendix is organized as follows: First we give a brief summary of the rocket LHC ion energization events, since they give the boundary conditions for the simulation. Next comes an introduction to the TICS instrument. Then we present the simulation procedure and discuss the statistical uncertainty and background noise level of the data. Finally we present some of the results from the simulations and discuss these. A general description of the Freja satellite has been given in section 1.9.1.

D.1 LHC ion energization observations by rockets

The Topaz III, Amicist, and Phaze II rocket observations represent most of the LHC ion energization events (LHC-I) observed by rockets and the following discussion is therefore based on the summary paper by Lynch *et al.* [1999]. All of these sounding rockets were

launched to an altitude of $\sim$ 1000 km in the pre-midnight auroral zone. Topaz III was launched in February 1991 during K_p=3, Amicist in February 1995 during K_p=1-, and Phaze II in February 1997 during K_p=4-.

The LHC-Is by rocket observations have shown the following properties:

- ion energization is correlated with localized lower hybrid wave events
- the ion energization is narrowly confined to 90° pitch angle ($\pm$10°)
- the thermal core of the ambient ion distribution is unaffected and has a temperature of roughly 0.1 eV
- the ion energization creates a high energy tail that is observed by the particle detectors from $\sim$1 eV up to $\sim$30 eV with a typical tail temperature ranging from 2 to 8 eV (the number of particles that is heated is therefore equal to the number of particles above 1 eV in a 0.1eV Maxwellian distribution)
- the scale size of the ion heated area is of the order of the ion gyro radius, and it is spatially wider than that of the wave event, ion energization is observed up to one gyro diameter outside the wave event
- only ions in gyro circles tangential to the edges of the wave event are accelerated by the wave
- O^+ is usually heated to higher temperatures than H^+
- the LHC ion energization is observed at a minimum altitude of 500 km, no maximum altitude is observed

D.2 The TICS instrument

TICS was one of the instruments in the Hot Plasma Experiment (F3H) [Eliasson *et al.*, 1994] on Freja. Figure D.1 shows the schematic of the TICS instrument by a vertical cut through its cylindrically symmetric aperture. It consists of a spherical "top-hat" electrostatic analyzer with 360° field of view followed by a cylindrically arranged magnetic momentum analyzer.

An electrostatic analyzer measures the energy per charge of incoming ions by letting them pass through a given electric field between two curved plates with different potential. This enables only particles with a centripetal force that balances the electrostatic force to pass through the instrument, i.e.

$$\frac{mv^2}{R_e} = qE, \tag{D.1}$$

where m, v, and q are, respectively, the mass, velocity and charge of the incoming particle, E is the applied electric field, and R_e is the radius of the curvature of the entrance path. This gives a constant energy per charge:

$$\frac{W}{q} = \frac{1}{2}ER_e, \tag{D.2}$$

where W is the kinetic energy ($\frac{1}{2}mv^2$) of the incoming particle. On TICS the electric potential bias on the spherical plates was stepped corresponding to particle energies from 1 eV to 5 keV, in 16 or 32 steps. Each energy step had a dwell time of 10 ms, and an energy sweep of

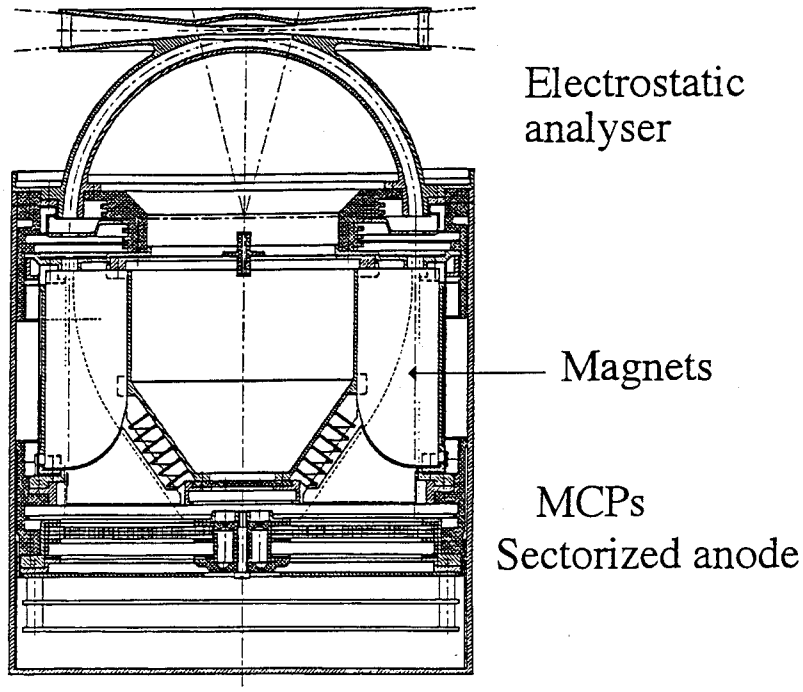

Figure D.1: Schematic of the TICS spectrometer on Freja. The different ion masses hit the MCP at different radial distances. (Figure from Eliasson *et al.* [1994].)

16 energies in 200 ms (40 ms for data handling). It could also be operated in constant energy mode with the advantage of higher temporal resolution. Three different energy levels were then used, corresponding to particle energies of 3.5 eV, 7 eV and 12 eV.

The magnetic momentum analyzer on TICS used a permanent magnetic field. A charged particle in a magnetic field will, as discussed in section 1.3, experience a Lorentz force,

$$\mathbf{F} = q\mathbf{v} \times \mathbf{B}, \tag{D.3}$$

where $\mathbf{B}$ is the magnetic field. This force is perpendicular to both the particle velocity and the magnetic field and results in a circular motion of the particle. Balancing the Lorentz force with the centripetal force we get a constant momentum to charge ratio

$$\frac{mv}{qB} = R_m, \tag{D.4}$$

where R_m is the radius of curvature of the particle trajectory. Particles with different masses experience different deflection in the magnetic field and will therefore be detected at different positions on the MCP detectors (Microchannel plates) in Figure D.1.

The plane covered by the TICS instrument was perpendicular to the spin plane, and the spin axis pointed towards the sun. This configuration gave a three-dimensional coverage in half a spin (3 seconds). Since the altitude of Freja was so low ($\sim$ 1700 km), the spin axis was perpendicular to the magnetic field during almost the whole orbit. Furthermore the satellite velocity was generally at an arbitrary angle to the spin axis. This resulted in a spin modulation in the count rate of TICS when one or more of the sectors ran into cold ions (i.e. when the relative ion velocity of cold ions, in the satellite rest frame, became detectable by

the instrument). This effect is called "ram" and it is generally seen twice in each satellite spin.

When the TICS instrument was operated in constant energy mode, the temporal resolution was high enough to examine the particle data inside individual density cavities (as observed by the wave experiment). One example of such data is shown in Paper III of this thesis. It is also clear that the TICS instrument was measuring in all directions in the right energy range to measure LHC-Is. The question that remains is whether the geometric factor of TICS is high enough to detect such events.

D.3 Simulation of the sensitivity of TICS

In the following we present a simulation of the sensitivity of the TICS instrument inside LHC-Is to see if such events are detectable by the instrument. The simulation is based on computer-codes developed by Patrik Norqvist [Norqvist *et al.*, 1998a] for the constant energy mode of TICS. The number of counts in the code, for given plasma parameters, is calibrated with the actual counts by TICS under the same conditions. The simulated number of counts thus reflects both the geometric factor and the S/N-ratio.

To simulate localized ion energization inside LHCs, as it would have been observed by TICS, a double distribution for number of counts is introduced. This is done by adding two Maxwellian distributions (one hot and one cold),

$$N(\mathbf{v}) = \sum_{s=3}^{32} [N_{hot}(\mathbf{v}(s)) + N_{cold}(\mathbf{v}(s))], \tag{D.5}$$

where the summation is over all sectors of the instrument. The geometry chosen is one with the magnetic field in the z-direction, spin-axis in the y-direction and satellite velocity in the xz-plane. Further a zero plasma drift velocity is chosen. This is a relevant approximation since the lower hybrid cavities are almost stationary [see e.g. Paper II of this thesis]. The hot and cold distributions are given by

$$N_{hot}(\mathbf{v}) = C \cdot \mathbf{v}^4 \left(\frac{n_{hot} \cdot e^{-\left(\frac{(v_x - V_{sat}\sin(\beta))^2 + v_y^2}{v_{th\perp}^2} + \frac{(v_z - V_{sat}\cos(\beta))^2}{v_{thz}^2} \right)}}{v_{th}^3} \right), \tag{D.6}$$

and

$$N_{cold}(\mathbf{v}) = C \cdot \mathbf{v}^4 \left(\frac{n_{cold} \cdot e^{-\left(\frac{(v_x - V_{sat}\sin(\beta))^2 + v_y^2}{v_{tc}^2} + \frac{(v_z - V_{sat}\cos(\beta))^2}{v_{tc}^2} \right)}}{v_{tc}^3} \right). \tag{D.7}$$

The variables are:

- n_{hot}, the number of particles in the hot distribution
- n_{cold}, the number of particles in the cold distribution
- v_{th} $(= \sqrt{v_{th\perp}^2 + v_{thz}^2})$, the thermal velocity of the hot particles (see definition below)
- $v_{tc} (= \sqrt{2\kappa T_{bgc}/m})$, the isotropic thermal velocity of the cold background particles

- V_{sat}, the satellite velocity, 7 km/s
- β, the angle between V_{sat} and the magnetic field
- $\mathbf{v}(s) = [v_x, v_y, v_z]$, the velocity of an incoming ion, as measured by one of the sectors on the instrument. The measured velocity depends on the energy level, E ($v \sim \sqrt{\frac{2E}{m}}$, were m is the ion mass), and also the line of sight of the sector, which varies during a satellite spin.
- C, a constant that contains e.g. the geometric factor. It is calibrated using the actual densities and counts measured by Freja.

The thermal velocity of the hot distribution (v_{th}) will have a different value inside LHC-Is (where it is supposed to be heated) than outside LHC-Is. We assume that the ion energization is only perpendicular to the magnetic field, i.e. in the x and y directions, as has been reported from rocket experiments. This is done by defining the thermal velocity of hot particles as:

$$v_{th} = \sqrt{2\kappa T_h/m}, \tag{D.8}$$

where $T_h = T_{cav}$ in the x- and y-directions inside LHC-Is and $T_h = T_{bgh}$ elsewhere (in the z direction inside LHC-Is and in all directions outside LHC-Is).

In the simulations we use a plasma density, n, as the sum of the densities of the hot and cold populations. It should be noted that the value of n is very important in this simulation since a large value of n will give a higher number of counts, and thus lower uncertainty in the measurements. We found it useful to define a new variable,

$$nc_{ratio} = \frac{n_{cold}}{n_{hot} + n_{cold}} = \frac{n_{cold}}{n}, \tag{D.9}$$

which is the proportion of particles in the cold population relative to the total density. This ratio thus gives the portion of the plasma that is unaffected by the energization inside LHC-Is.

The simulation can be carried out for both hydrogen and oxygen, but here we concentrate on oxygen ions, since O^+ energization was more efficient than H^+ energization according to the rocket observations. We also note that the study by Ergun *et al.* [1995] indicates that bulk energization of H^+ and tail energization of O^+ might result from energization by lower hybrid waves. The perpendicular width of the resulting density depletion will, however, be controlled by the O^+ energization. It is also important to note that probably 90 % of the ions (in number density) at Freja's altitude are oxygen ions.

Ninety five (95) LHC-Is were included in the simulation for a time sequence of 12 seconds (two satellite spins). Each cavity in the simulation was assumed to be detected during a time period of $\sim$ 10 ms. The time-period is determined by the satellite velocity, since the LHCs are nearly stationary on this time scale (see e.g. Paper I). This 10 ms is also the dwell time for each ion sample by TICS and thus it gives the instrument's highest possible resolution.

D.3.1 Statistical uncertainty and background noise

All measurements have a statistical uncertainty. It can be argued that the number of counts in one time interval, N, follows a Poisson distribution if we assume that the counts are independent and randomly distributed in the given time interval. The standard deviation in a Poisson distribution is known to be $\sqrt{\bar{N}}$, where $\bar{N}$ is the mean value of number of

counts [Squires, 1993]. For a large $\bar{N}$, a Normal distribution with mean value $\bar{N}$ gives a good approximation to the Poisson distribution [Bhattacharyya and Johnson, 1977]. The probability of a given count rate being inside an interval of one standard deviation $[\bar{N} - \sigma, \bar{N} + \sigma]$, in a Normal distribution is 68 %. The probability of being inside the interval two standard deviations in a Normal distribution $[\bar{N} - 2\sigma, \bar{N} + 2\sigma]$, is 95 %, and the probability of being inside less than three standard deviations from the mean value $[\bar{N} - 3\sigma, \bar{N} + 3\sigma]$, is 99.7 %.

The measured value of N is, in practice, often used as an estimate for the mean value, giving a standard deviation in the measurement of $\sqrt{N}$. This gives an uncertainty in the measured count rate of typically $\pm 2\sqrt{N}$ (within 95 % probability) or $\pm 3\sqrt{N}$ (within 99.7 % probability).

For the possible ion energization inside LHC-Is discussed here we thus find that the related peak in count rate has to be more than $2\sqrt{N}$ higher or lower than the background count rate (outside the cavity) to prevent confusion with background fluctuations. (Note that this localized ion energization may be detected both as an increase or as a decrease in the count rate, due to satellite motion.) In the following we therefore calculate the ratio, R, between the peak in count rate above or below background inside LHC-Is, N_c, and the standard deviation of the background count rate, N_{bg},

$$R = \frac{N_c}{\sqrt{N_{bg}}}. \tag{D.10}$$

An $|R|$ value greater than 2 thus gives a peak greater than two standard deviations.

A high $|R|$ value does not, however, necessarily mean that the peak is significant since there is always background noise due to unwanted particles and cosmic radiation that enters the instrument. These disturbances will vary during a satellite orbit as it encounters different plasma environments. As an example, the radiation belt severely affects the count rate of TICS as the high energy (MeV) electrons directly enter the instrument. However, we find the noise level of TICS to be much less than 1 count/10 ms when the satellite is far away from the radiation belts. A maximum noise level of 1 count/10 ms will therefore be used in the following simulation.

D.4 Results

Figure D.2 shows the simulated count rate by the TICS instrument (following Eq. D.5) for the parameters given in Table D.1. The plasma density, n, is chosen according to the plasma environment at Freja's altitude. The portion of plasma that is unaffected by the energization, nc_{ratio}, the temperature of the hot and cold populations outside the LHC-Is, T_{bgh} and T_{bgc}, and the temperature inside LHC-Is, T_{cav}, are chosen according to the rocket observations discussed above. The angle between V_{sat} and B, β, is chosen arbitrarily.

Some of the 95 LHC-Is included in the simulation can be seen in Figure D.2 as narrow spikes over or under the sinusoidal background variation. The background variation is due to ram caused by the satellite spin motion through the plasma. A band of two standard deviations $[-2\sqrt{N_{bg}}, 2\sqrt{N_{bg}}]$ around the background, including the background noise level is marked gray to visualize the uncertainty in the measurement. Only those spikes that are seen outside this shaded area are significant.

For the plasma parameters chosen in these simulations the possible ion energization inside LHC-Is is most easily observed when the instrument is at the 12 eV energy level. This

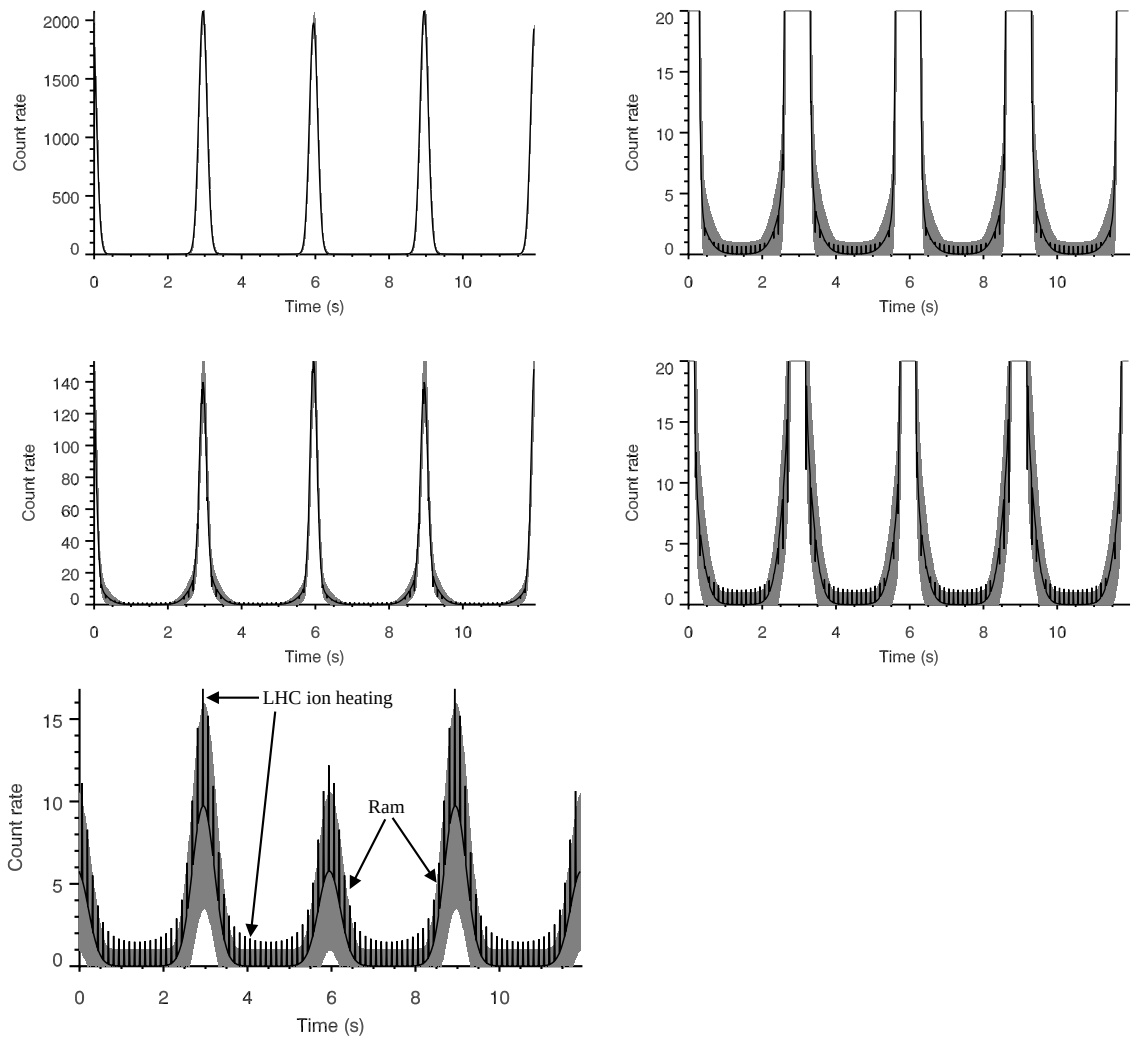

Figure D.2: Simulated counts of ions by the Freja TICS instrument in constant energy levels of 3.5 eV (upper), 7 eV (middle), and 12 eV (lower) over two satellite spins (= 12 s). The count rate is in counts/10 ms (it should be multiplied by 100 to get counts/s) and it is based on the actual geometric factor of the TICS instrument. The left hand panels give a close-up of the right hand panels for low count rates. The plasma parameters are the same in all simulations and are given in Table D.1. In total 95 LHC-Is are included in all of the simulations, and the narrow peaks (seen most clearly in the lowest panel) indicate ion energization inside LHC-Is. Note that the four large peaks are due to ram caused by the satellite motion. A band of $N \pm 2\sqrt{N}$ and also the background noise level are marked gray, indicating the uncertainty in the measurement.

can be explained by the fact that this energy level is the one that measures the less cold background since it is the highest energy. For the two other energy levels will a larger part of the background ram into the instrument, and the relative contribution from LHC-I events is thus smaller. The satellite velocity (7 km/s) corresponds to a particle energy of $\sim$ 4 eV (for oxygen ions). It is also evident that the peaks are most easily observed when the instrument

Table D.1: Parameters used in the simulation.

n, density	500 cm^{-3}
nc_{ratio}, cold portion	0.90
T_{bgh}, hot background temp.	1 eV
T_{bgc}, cold background temp.	0.1 eV
T_{cav}, temp. inside LHC-Is	8 eV
β, angle between $\mathbf{V}_{sat}$ and $\mathbf{B}$	90°

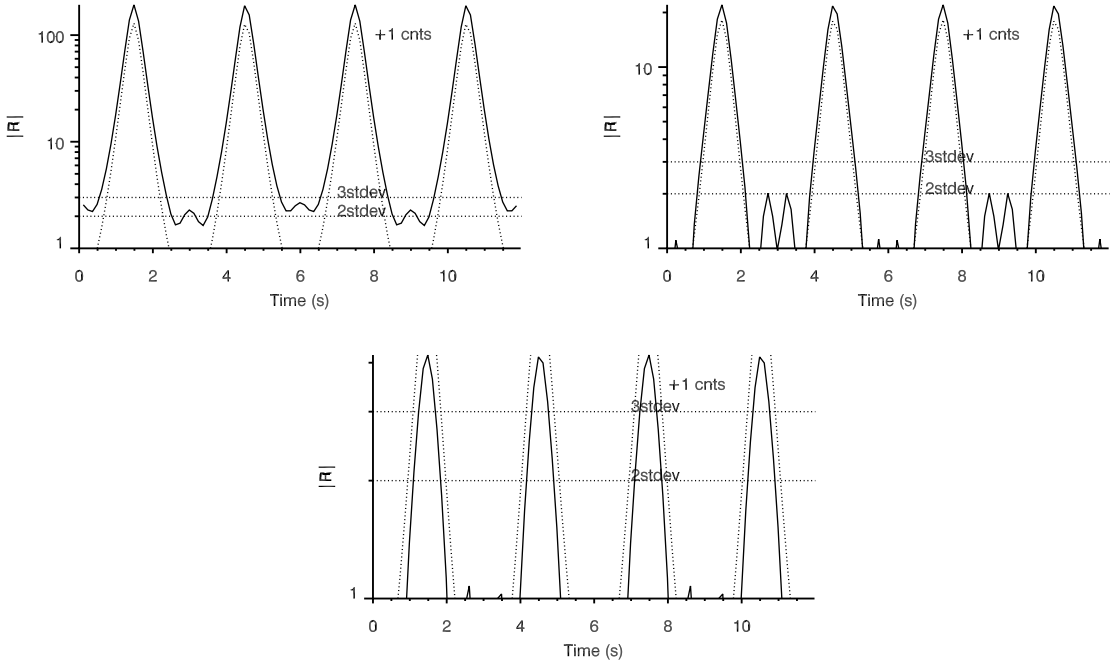

Figure D.3: Variation of $|R|$ during two satellite spins for the energy levels: 12 eV (upper left), 7 eV (upper right), and 3.5 eV (lower) under the same conditions as for Figure D.2. Horizontal dashed lines show the levels of corresponding to 2 and 3 standard deviations. The other dashed line shows the background noise level.

is measuring in the negative ram direction (i.e. when all sectors of the instrument are looking perpendicular to the satellite velocity). This is seen as valleys in the background in Figure D.2.

To give an even better visualization of this, Figure D.3 shows the variation of $|R|$ (defined in Eq. D.10) during two satellite spins for the three energy levels of TICS. The plasma parameters in Table D.1 are also used here. The $|R|$-values drastically vary with the spin-phase, as we have expected. The dotted lines in the plots give the three and two standard deviation levels and also the background noise level.

Table D.2 shows the total number of LHC ion heating events (out of 95) with R greater than 2 and 3 (2 or 3 standard deviations) that are detected by TICS during two satellite spins for the cases shown in Figure D.3. Values are listed for all three energy levels. Apparently the 12 eV energy level is the most successful one in detecting ion energization inside LHC-Is. In total 85 out of the 95 LHC-Is can be detected above two standard deviations and 58 of them can be detected above three standard deviations. The 7 eV energy level may detect

approximately half of the LHC-Is above two standard deviations and one third above three standard deviations. The lowest energy level, 3.5 eV, will not detect any LHC-Is above two standard deviations.

The detection rate is expected to vary for various plasma-parameters different from those in table D.1. We will therefore in the following calculate the detection rate of LHC-Is for different plasma parameters. The criteria for detection in the simulation is that the count rate inside LHC-Is has to be above the noise level and also above the statistical uncertainty ($|R| > 2$).

The variation in detection rate of LHC-Is (in percent) for varying plasma temperatures (T_{bgc}, T_{bgh}, T_{cav}) is shown in Figure D.4. The position in the plots that corresponds to the plasma parameters in Table D.1 is marked with an asterisk. The plots show very complex signatures, but we still see a high probability of detection of LHC-Is at the 12 eV energy level. With the instrument at the 12 eV energy level, LHC-Is with temperatures (T_{cav}) between 6 and 10 eV will be easily observed (detection rate $> 75\%$). This is when the LHC-I ion energy, ε, fits to the detection energy at ram, i.e. when $\varepsilon + 4$ eV ≈ 12 eV since the satellite velocity corresponds to 4 eV. We recall that the ions are Maxwell distributed so the countrate of LHC-I ion energies close to this energy is also high. In the negative ram direction will the LHC-I ions give a large contribution at the 12 eV energy level even for LHC-I ion temperatures down to 6 eV since the high energy tail of this population will be detectable there.

The hot background temperature (T_{bgh}) should, correspondingly, be higher than the cold background temperature but lower than 1.1 eV. The first results from the fact that T_{bgh} gives and important contribution to the countrate inside LHC-I events (v_z). N_c therefore decreases for T_{bgh} close to T_{bgc}, giving lower R. Too high T_{bgh} will, on the other hand, give higher contribution from the background (higher N_{bg}) and thus lower R. We note also that 100 % of the LHC-Is will be detected above the noise level and 2σ if the cavity temperature is above 8 eV and the hot background temperature is between 0.2 and 0.6 eV, where all the other parameters are given in table D.1.

The cold background temperature should preferably be below 0.3 eV to be detected with a detection rate $> 75\%$ for the 12 eV energy level, and less than 0.1 eV for the 7 eV energy level. This is because a high cold background temperature will enable detection of more cold background ions (increasing N_{bg}), thus decreasing R. The detection rate for the 3.5 eV energy level is close to zero (the highest value is 9% at the lowest values of T_{bgh}) or zero for the energy ranges shown in Figure D.4 since the relative contribution from IHC-I ions is small compared to the background for the lowest energy levels.

Figure D.5 shows the variation in the detection rate of LHC-Is, as a function of the temperature inside LHC-Is, for different angles between the satellite velocity and the magnetic field, β. We see a preference for β around 90°, and note that the small asymmetry below and

Table D.2: Total number of LHC ion heating events with $|R|$ greater than 2 and 3, and a count rate above the noise level, if detected by TICS in the different energy levels during two satellite spins.

Energy level	$\|R\| > 2$	$\|R\| > 3$
12 eV	85/95	58/95
7 eV	46/95	36/95
3.5 eV	0/95	0/95

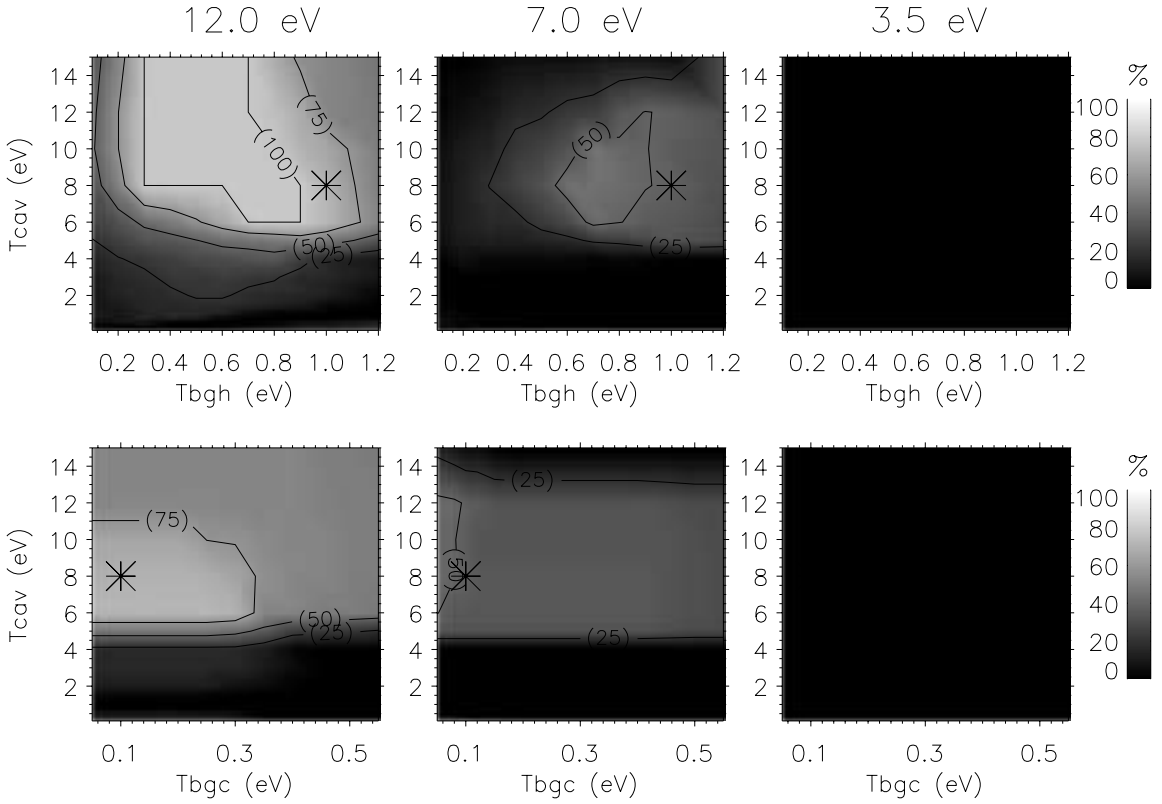

Figure D.4: Variation in detection rate of LHC-Is in percent for varying plasma temperatures. The three energy levels are shown in the left- (12 eV), middle- (7 eV), and righthand (3.5 eV) panels respectively. The upper (lower) panels show detection rate as a function of background temperature of the hot (cold) population and the temperature inside LHC-Is. The point corresponding to the values of Table D.1 is indicated in each plot for comparison.

above 90° seen in Figure D.5 is caused by the distribution of LHC-Is chosen in the simulation (8 LHC-Is during 1 sec.) since their position relative to the ram will vary with β. This figure also shows the variation in the detection rate of LHC-Is for varying portions of cold plasma, nc_{ratio}, and different temperatures inside LHC-Is. The nc_{ratio} should be as low as possible to detect LHC-Is. This is rational, since if more particles are heated (corresponding to lower nc_{ratio}), the energization will also be more easily detected. The detection rate is, however, rather high (100 % for the 12 eV level, $> 50\%$ for the 7 eV level, and $> 25\%$ for the 3.5 level) until nc_{ratio} reaches 0.85, when it drops steeply towards zero.

Figure D.6 shows the variation in detection rate of LHC-Is in percent for varying density, n. The detection rate increases with increasing density, since a lower density will cause fewer particles to be detected by the instrument. If fewer particles are detected, the relative error will be higher and we also get closer to the noise level. Both N_c and N_{bg} in Eq. D.10 will be proportional to the density, thus giving R proportional to $\sqrt{n}$. To be inside the 100 % detection rate at the 12 eV energy level, the density must be higher than 750 cm^{-2} for all other parameters given in Table D.1. To be inside 75 %, a density above 400 cm^{-2} is needed. At the 7 eV energy level, a density of 400 cm^{-2} will only give a 25 % detection rate, while at

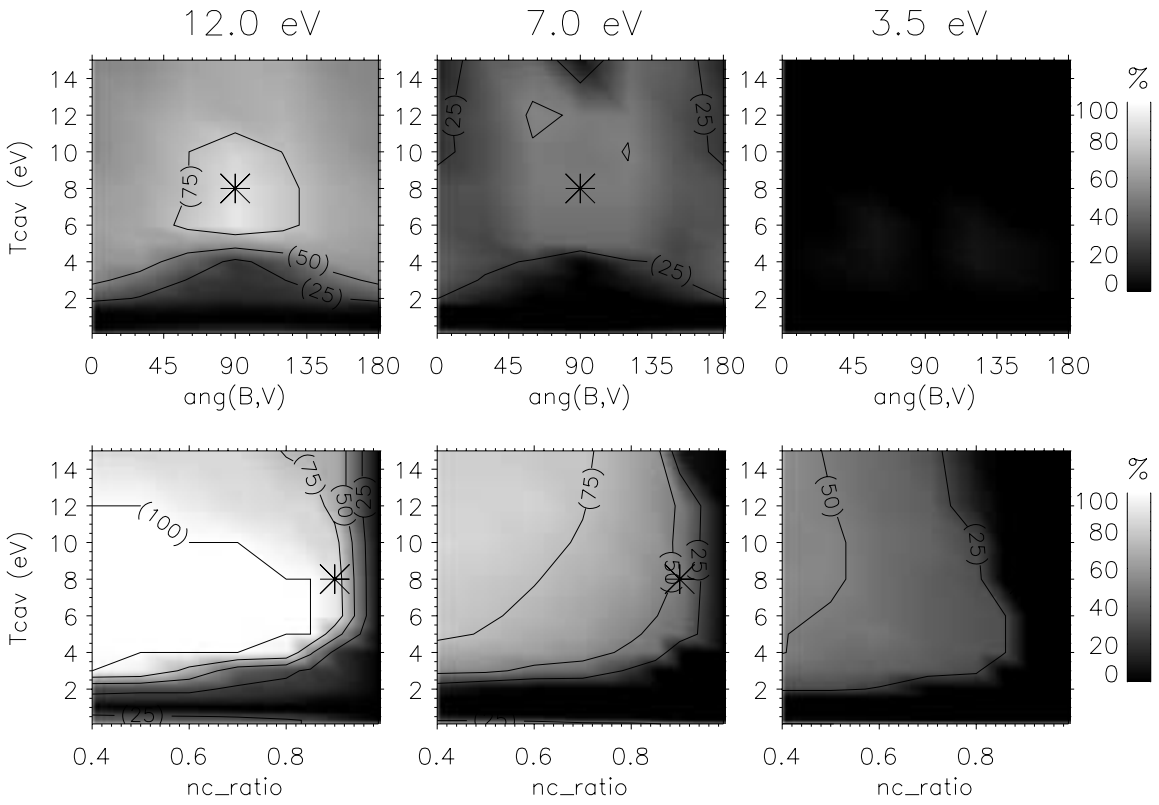

Figure D.5: Variation in detection rate of LHC-Is in percent for varying angles between the satellite velocity and the magnetic field (upper panels) or portion of cold plasma, nc_{ratio}, (lower panels) for varying temperatures inside LHC-Is. The three energy levels are shown in the left- (12 eV), middle- (7 eV), and righthand (3.5 eV) panels respectively. The point corresponding to the values of Table D.1 is indicated in each plot for comparison.

the 3.5 eV energy level it will be close to zero.

D.5 Summary

Lower hybrid density LHC-Is are observed both by rockets and satellites, but correlated ion energization is only seen in the rocket observations. The simulations herein show that possible ion energization inside lower hybrid LHC-Is (LHC ion energization) should also be observable by the TICS instrument on Freja when it is operated in constant energy mode with energy levels of 12 eV or 7 eV. For the most probable plasma conditions (as listed in Table D.1) TICS should be able to detect 85 out of 95 possible LHC-Is (i.e. events that have count rate above two standard deviations and also above the noise level) when it is operated at the 12 eV energy level, 46 out of 95 LHC-Is at the 7 eV level, but none at the 3.5 eV energy level. The total probability of detection is then

$$P = P_{N2\sigma} \cdot \frac{N_{|R|>2}}{N_{total}}, \tag{D.11}$$

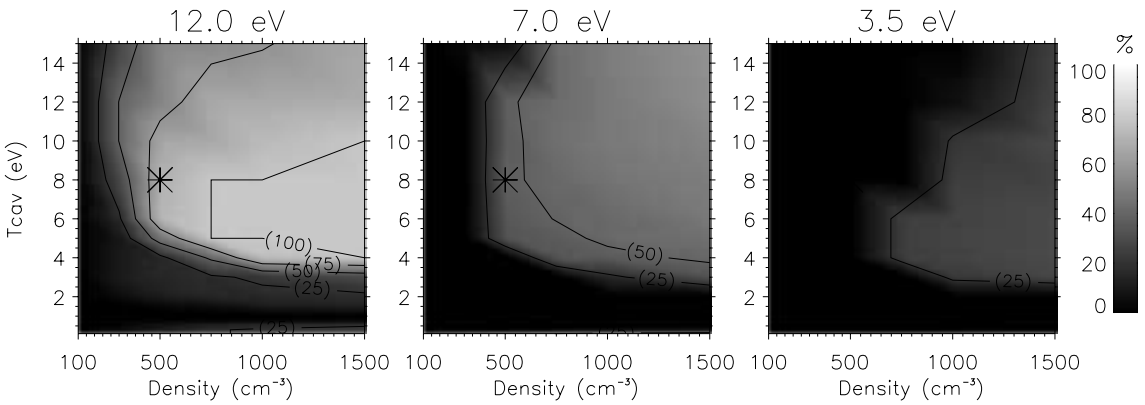

Figure D.6: Variation in detection rate of LHC-Is in percent for varying density. The three energy levels are shown in the left- (12 eV), middle- (7 eV), and right-hand (3.5 eV) panels respectively.

where $P_{N2\sigma}$ is the probability of being inside two standard deviations of a Normal distribution (that is 95.4 %) and $N_{|R|>2}$ is the number of LHC-Is detected above noise level (i.e. the count rate is high enough) and with $|R| > 2$. This gives a total probability of detection of 85 % at the 12 eV level, 46 % at the 7 eV level, and 0 % at the 3.5 eV level. It should be noted that this yields for the chosen plasma conditions (table D.1). We have in this simulation mainly used $nc_{ratio} = 0.90$ (i.e. 10 % of the plasma is heated). If a smaller portion of the plasma is heated (larger nc_{ratio}), the detection rate will be significantly lower (see Figure D.5). For a background plasma with a temperature of 0.1 eV, a tail plasma population which is heated from 0.2 – 0.6 eV to 6 – 10 eV inside LHCs is the most easily detected by TICS. These temperatures give detection rates comparable to those given above, or even higher. We note that a cold plasma at Freja altitudes is typically 0.2-0.5 eV [Norqvist *et al.*, 1998a], and not 0.1 eV which is measured by rockets at lower altitudes. This might give somewhat lower detection rates as seen in the lower panels of Figure D.4. We also note that the detection rate will vary during the satellite orbit since the angle between the satellite spin-axis and the satellite velocity will vary.

The detection rates are strongly dependent on the density. A decrease in the density from 1000 cm^{-2} to 400 cm^{-2} will decrease the detection rates at the 12 eV energy level from 100 % to 75 %, at the 7 eV energy level from above 50 % to 25 %, and at the 3.5 eV energy level from 25 % to close to 0 %. Plots of the plasma density inside regions that contain lower hybrid LHC-Is, in two different Freja orbits, are given in Figure A.1 in Appendix A. The plasma density in these orbits varies from 150 cm^{-2} to 700 cm^{-2} inside the areas of LHCs, and the detection rate will thus vary greatly. The density used in the simulation is the density of oxygen ions, which is generally only a portion of the total plasma density. A reasonable assumption is that 90 % of the ions are oxygen ions at Freja's height. The oxygen density is thus 140 – 630 cm^{-2}. The plasma density inside LHC-Is is on average 2.1 % below the background density.

D.6 Discussion

This simulation indicates that the Freja TICS instrument is capable of measuring LHC-Is similar to those reported from rocket experiments, at least when TICS is measuring at the 12 eV energy level under optimal observation circumstances: i.e. the satellite must be well away from the ring current (to get a low noise level) and the satellite should be moving perpendicular to both the magnetic field and the spin axis. These circumstances are most likely fulfilled for times when Freja observes LHCs, although a more detailed study of all available Freja-data is needed. We note that the ion data shown in Paper III are from the 12 eV energy level, and Freja should thus have detected ion energization if there was any.

As a result of this simulation the lack of LHC-I observations by Freja has to be explained by real physical mechanisms. We may point out three fundamental differences between the rocket and satellite measurements:

(1) The altitude difference between the rocket (1000 km) and satellite (1700 km) observations gives differences in density, temperature, and ion composition.

(2) Almost all of the LHCs observed by Freja are seen in the pre-noon sector and they are nearly absent in the pre-midnight sector (Paper I), while all the LHC-I observations by rockets are seen in the pre-midnight sector. Therefore, Freja might have observed different types of LHCs. In fact rocket experiments in the pre-noon sector have not shown the same LHC ion energization.

(3) The LHC-Is might have different scale size at different heights due to the difference in the magnetic field strength. The scale size relative to the wavelength of the lower hybrid wave might therefore differ with height.

We do not, however, see any clear physical mechanism that can explain the observed difference between the rocket and satellite observations. This needs further investigation.